A high-resolution coupled ice-ocean model of winter circulation on the Bering Sea Shelf. Part II: Polynyas and the shelf salinity distribution

Scott M. Durski[1]

Alexander L. Kurapov[1,2]

[1] College of Earth, Ocean and Atmospheric Sciences, Oregon State University

[2] National Oceanic and Atmospheric Administration, Coast Survey Development Laboratory, Silver Spring, MD

Abstract

The sea ice component of a regional high-resolution ocean model is improved, with particular attention to accurate representation of the salinity budget for the coupled system. The impact of this improvement is shown first using a one-dimensional test and then the realistic model simulation of the Eastern Bering Sea for the relatively high sea ice extent winter of 2009-10. Improvements to the model ice-ocean salt flux parameterization are demonstrated by comparison of model shelf salinity fields with observations from moorings and CTDs. As polynya regions can strongly influence winter salinity distributions on the Bering Sea shelf, model ice concentrations are compared to satellite estimates for several regions. Areas with a tendency to exhibit higher than average winter open water area include St. Lawrence Island and the southern coast of the Chukotka Peninsula. A new methodology is proposed analyzing the evolution of the salinity distribution with the aid of salt flux tracers that track occurrence of brine and meltwater separately. These demonstrate how cold winters on the Bering Sea shelf are characterized by a freshening and stratifying of the mid- to outer- shelf and an increase of salinity on the inner shelf. Use of an ice-age tracer in the model reveals an anticyclonic circulation of sea ice in mid-winter, as the Bering slope current and Anadyr current recirculate ice that has been transported south-southwestward by the predominant winds. The characteristics of coastal polynya regions are quantitatively compared and a model transect extending from the St. Lawrence polynya to the shelf break is analyzed to help illustrate the temporal and spatial variability of stratification and circulation occurring as the sea ice advances and retreats over the winter season.

1 Background

The Eastern Bering Sea shelf is the largest shelf sea in the world south of the Arctic ocean. From north to south it spans nearly 1300 km from the Bering Strait, where the shelf exchanges waters with the Arctic Ocean, to Unimak Pass of the Aleutian Island arc, where direct exchange with the Pacific Ocean occurs. In the zonal direction, from the Alaskan coastline to the shelf break, the shelf is nearly as wide as it is long, extending over 900 km in some places. As the only ocean exchange between the Pacific and Arctic, with Arctic sea ice rapidly in retreat, the northern Bering Sea shelf is becoming part of an increasingly alluring trade route between Asia and Northern European countries. But beyond its potential future importance to shipping, this vast coastal shelf system already supports some of the largest commercial fisheries in the world while also supporting diverse ecosystems that provide critical habitat for a wide variety of marine mammals and sea birds.

Sea ice plays an important role in the habitat structure of the Bering Sea in all seasons despite forming typically in late fall and melting in the spring (Hunt and Stabeno, 2002; Stabeno et al., 2012a, 2012b). In cold years, the sea ice spreads southward covering nearly the entire shelf area. Even in moderate years, spring melt on the northern shelf contributes significantly to the stratification in the summer season (Ladd and Stabeno, 2012; Stabeno et al., 2012a). But in some recent winters, such as in 2018 and 2019, there was little sea ice at all beyond shallow portions of some of the northernmost coastlines. The melting of sea ice regularly leads to the formation of a bottom cold pool over the central and southern shelf that constrained walleye pollock and pacific cod populations(Thorson et al., n.d.). Years without sea ice, and consequently without the cold pool have led to northward migration of those species, causing Arctic cod to disappear from the Northern Bering Sea shelf where previously they were in abundance. There was significantly more sea ice in the winter of 2020 than in the previous two years but over the prior decade, the overall trend was negative.

Pressing questions persist as to the rate of change and amount of variability to expect in the coming years. Part of the answer to these questions depend on understanding the ice-melt cycle in the Bering Sea and the impact of variability of this on shelf stratification and circulation. Since the stratification in this area is largely defined by salinity, this becomes a question of how salt becomes redistributed over the shelf in the winter months.

The salinity field on the broad shallow Bering Sea shelf can change dramatically in cold winters, when sea ice growth is extensive. In late fall, the cross-shore salinity gradient is directed offshore, driven by freshwater coastal influx from rivers and entrainment of saltier Bering Sea Basin water along the shelf break. But over the winter ice production and brine rejection tend to be highest close to the northern Bering Sea coastlines. Due to prevailing wind patterns, much of the sea ice produced in these regions in cold years is advected to the mid- or outer- shelf before it melts. The net effect of the winter variability can be a large-scale redistribution of shelf salinity over the winter season. Salinity gradients also develop at smaller spatial scales as the particulars of wind direction and coastline orientation determine regions of enhanced and reduced ice production both along the continental coastlines of Alaska and Russia and those of the shelf islands such as St. Lawrence, St. Mathew, Nunivak (to locate these and other geographic features specified in the manuscript, refer to Figure 1a).

Observational studies have led to a variety of insights related to salinity redistribution on the Bering Sea shelf. The overall pattern of an ice conveyor belt, ice formation in the northern Bering Sea, southward transport by prevailing northerly winds and subsequent melt on the southern and outer shelf, were presented by Pease (1980). The role of polynyas has long been recognized as well (Schumacher et al., 1983; Stringer and Groves, 1991). More recent observations related to the redistribution of salinity include those of Danielson et al. (2006) who examined mid-shelf circulation south of St Lawrence Island with 14 years of mooring data and oceanic drifters, finding that brine rejection from the polynya competed with westward advection of fresher, presumable riverine influenced, water leading to high variability in the region and no clear signature of a dense water plume. Sullivan et al. (2014) studied the evolving relationship between sea ice and water column structure using ice cores, satellite data and four moorings distributed over shelf along the 70m isobath, noting latitudinal differences and emphasizing the role melt dynamics played in determining subsequent stratification..

Not surprisingly there are many challenges to collecting comprehensive hydrographic information over an area as expansive and heterogenous as the Eastern Bering Sea shelf particularly in winter.Numerical circulation models have been a valuable tool for estimating the ocean structure and dynamics on the Bering sea shelf over larger spatial and temporal scales than could not be achieved observationally. Most commonly, for the Bering Sea, coupled ice ocean models have been used to study interannual variability. Clement et al.(2005) examined interannual variability in transports over the northern shelf over a 23 year period and Clement-Kinney et al.(2009) examined shelf slope exchange on a similar time scale. Variability in the southwesterly transport of sea ice over a 39 year period has been studied (Zhang et al., 2010) along with the related issue of year-to-year variability in the cold pool extent over the same period (Zhang et al., 2012). Cheng et al. (2014)examined nearly 100 years of a climate model output finding that high ice-extent years led to more saline water in the northern Bering Sea and fresher water to the south and on the outer shelf. Kawai et al. (2018) used a coupled atmosphere-ocean-ice model to explore the correlation between sea surface salinity on the northwestern portion of the Bering Sea shelf and Arctic sea surface heights. Here again the focus was on interannual variability utilizing 56 years of model simulation.

These projects have led to a much better understanding of the large year-to-year changes observed in the Bering Sea, but due to the computational costs of such lengthy calculations over a large area, they have necessarily neglected a careful examination of the accuracy of their solutions at higher temporal and spatial resolutions that can be relevant to navigation and fisheries applications. The approach being taken in this study, which is a continuation of our earlier work (Durski et al., 2016; Mauch et al., 2018; Durski and Kurapov, 2019) is to develop and refine the model performance through careful inspection of the simulation quality for a particular year, on time scales of days-to-weeks rather than years and on spatial scales of tens of kilometers rather than hundreds. Throughout this work we have found that model refinements emerge as a result of the close evaluation, representing genuine physical improvement rather than tuning.

In part 1 of this study (Durski and Kurapov, 2019), refinements were made to the sea ice component of a coupled ice ocean circulation model in order to improve the model skill at capturing the seasonal advance and retreat of the sea ice in the Bering Sea. Comparisons were performed for the winter of 2009-2010 both because of the availability of observational datasets and because it in turn followed on a study of ice-free circulation for the summer of 2009 (Durski et al., 2016). The model succeeded in capturing the timing, evolution, and movement of the eastern Bering Sea ice cover. It also reproduced coastal polynyas with reasonable timing and areal extent.

In this study, focus is turned to the ocean structure below the ice and in particular to the evolution of the shelf salinity. Observational comparisons are made with moorings, CTD data and satellite products. Spatial and temporal distributions of polynyas and their associated brine rejection are examined in much greater detail than has been presented previously. Novel model tracers are used to track where melting/brine injection occurs and where these altered water parcels advect over the winter season. The high model temporal and spatial resolution also allows examination of the evolution of both the ice thermodynamics and the underlying stratification and circulation on a transect that extends from polynya to shelf break. Ice circulation is examined through the use of an ice-age tracer, offering a perspective beyond that provided by the traditional conveyor belt model.

As the focus of this study is on salinity distributions, a necessary requirement is that the model accurately estimates the salt fluxes associated with sea ice formation and melt. As will be discussed below, the formulation in the ice model used in part 1 of this study was inadequate for these purposes because it deviated significantly from conservation of salinity over the freeze-melt cycle. Typically the principle concern in salt flux parameterizations for coupled ice ocean models is to accurately estimate ice salinity and the flushing of brine channels during spring melt because these features can play a very significant role in accurately representing the ice dynamics and thermodynamics. But they may not be commensurate with accurate representation of the ocean salinity beneath. Here, we replace the ice-ocean salt flux parameterization used in part 1 with a straightforward, much more conservative scheme and demonstrate the improvement for the ocean state estimate it offers.

Descriptions of the modeling and the observations used in this study are laid out in Section 2. This includes a short discussion of changes to the sea ice model surface salt flux parameterization. Detailed explanations of these changes can be found in Appendix A and a one-dimensional case study to demonstrate the effect of those changes is presented in Appendix B. Section 3 compares the coupled model with satellite, mooring and profiler data. For 2009-10, the year that this study focuses on, the existing data comes primarily from broadly spaced shelf moorings targeted at capturing the large-scale temporal and spatial patterns and tightly spaced Bering Strait moorings, useful primarily for estimating exchanges with the Arctic. The objective here is to first demonstrate that our high-resolution model reasonably reproduces the observable fields, and then use it as a tool for elaborating on the ocean structure and dynamics in the many places where the observations do not reach. In section 4, model results focused on the winter redistribution of salinity and the role of polynyas in that process are presented and analyzed. This is followed by a summary discussion in Section 5.

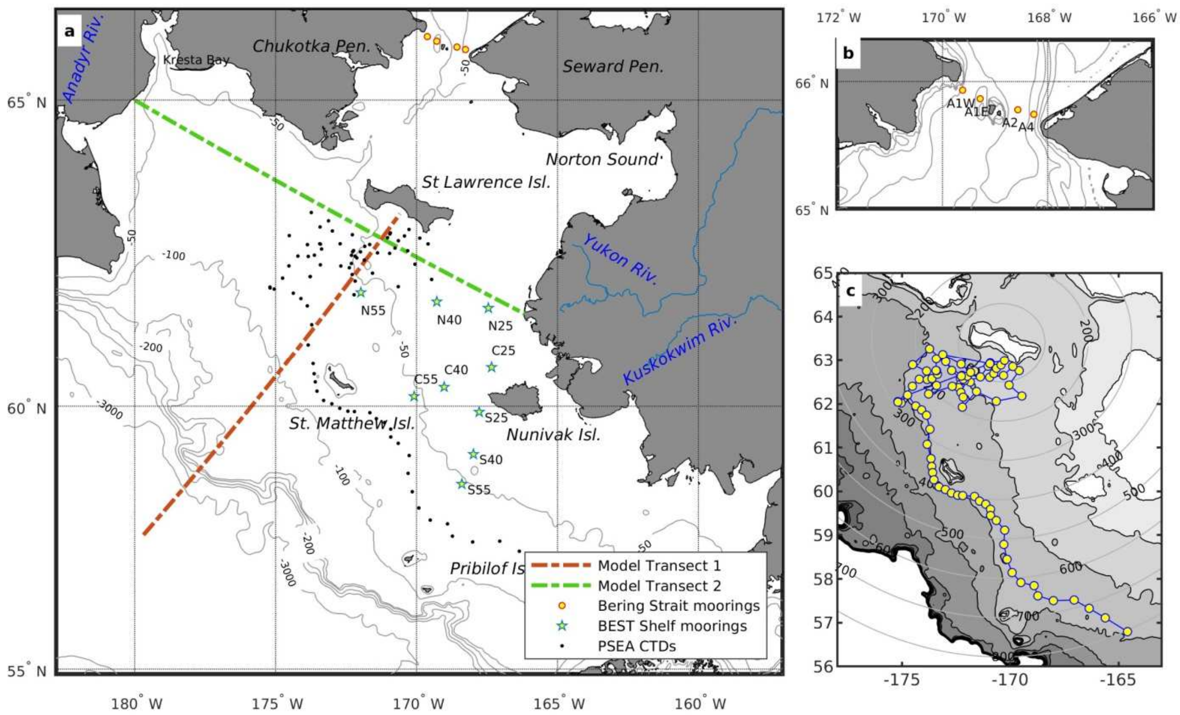

Figure 1. **a** *Map of the eastern Bering Sea shelf portion of the model domain. Dashed lines mark transects analyzed in the model. Observational mooring locations used for model-data comparisons are also indicated.* **b** *Zoom of the Bering Strait mooring locations; bathymetric contours are every 10 m* **c** *The cruise track map and positions of the PSEA CTD profiles; concentric circles indicate distance in km from the center of the southside of St. Lawrence Island.*

2 Methods and data

Much of the numerical model setup, and some of the satellite data analysis in this study inherits directly from part 1 of the study (Durski and Kurapov, 2019) . A very similar model setup was used for a study on summer circulation in the eastern Bering Sea (Durski et al., 2016) and a study of transport through the eastern Aleutian islands (Mauch et al., 2018). A brief overview of the set up and differences from the previous model setups are described in this section. For further details please refer to the earlier works.

2.1 The ROMS numerical model setup

2.1.1 ROMS base configuration

Simulations are performed using the Regional Ocean Modeling System (ROMS, http://www.myroms.org) in a model domain that spans the region zonally from 178°E to 157°W and meridionally from approximately 50°N to 66.4°N. The model horizontal grid spacing is approximately 2 km. 45 terrain-following levels are used in the vertical direction. The model includes tides, atmospheric forcing from the North American Regional Reanalysis (NARR) (Mesinger et al., 2006), open boundary conditions from a global HYCOM solution. Climatological freshwater inflows from the Yukon, Kuskokwim and the Anadyr rivers are added, distributed over depth and horizontally as point sources over the grid points along the coastlines in the vicinities of the river mouths.

In the previous publications the model ocean fields were initialized on June 1, 2009 using outputs from the 0.08° resolution Navy global model (HYCOM GLB[au]0.08 (Chassignet et al., 2007), http://www.hycom.org) for the Bering Sea basin melded with a BESTMAS regional simulation solution (Zhang et al., 2012, 2010) on the shelf. However, in analyzing fall shelf salinity fields for this study, it was found that the salinity initialization provided for the summer/fall simulation left unrealistically high salinity waters on the inner to mid- shelf along much of the Alaskan coast north of Nunivak Island. In order to correct for this, Bering Shelf mooring data (to be described more in Section 2.4) was used to estimate the June 2009 shelf average salinity in ice-free areas inshore of the 60m isobath. The new initialization generated was identical to the original initialization in Durski et al. (2016) for June 1 2009, other than the adjustment of the salinity inshore of the 60m isobath along the Alaskan coast to a depth-uniform value of 31.1. This was smoothly melded to the previously generated initial salinity field farther offshore. With this new initialization, a new summer/fall ice-free spin-up simulation was performed to generate the November 1 initialization file for the series of winter simulations discussed here. These ran through July 2010.

2.1.2 ROMS tracer fields

Several tracer fields are utilized in this study for diagnostic purposes. In order to track the migration of ice across the Bering Sea shelf, an age tracer was added to the ice model (similar to that in Harder and Lemke, 2013). The age tracer obeys the prognostic equation

$$\frac{D(A_i h_i)}{Dt} = h_i - A_i max\left(\left.\frac{\partial h_i}{\partial t}\right|_{Th}, 0\right), \qquad (1)$$

where A_i represents the average age of the ice within a cell, h_i the cell-averaged ice thickness and $\frac{D}{Dt}$ the total derivative (computed using two-dimensional ice velocity). In this equation, $max\left(\left.\frac{\partial h_i}{\partial t}\right|_{Th}, 0\right)$ denotes the portion of the increase in ice volume due to thermodynamic processes only. The second term in (1) acts to reduce the ice age in a grid cell when new ice forms. There is an assumption here that ice is ‘well-mixed’ within a grid cell, such that melting does not affect the age of the ice in a cell, while in actuality the most recently formed ice is likely the earliest to melt.

Tracers are also added to the ocean model, to aid in identifying the distribution of brine injection and meltwater. The accumulation, transport and mixing of each is represented by

$$\frac{DP^+}{Dt} = \frac{\partial}{\partial z} K_S \frac{\partial P^+}{\partial z} \qquad (2)$$

$$\frac{DP^-}{Dt} = \frac{\partial}{\partial z} K_S \frac{\partial P^-}{\partial z} \quad (3)$$

$$\frac{DP}{Dt} = \frac{\partial}{\partial z} K_S \frac{\partial P}{\partial z} \quad (4)$$

where the surface boundary condition on P^+ , P^- and P are $max(F_S, 0)$, $min(F_S, 0)$ and F_S respectively, with F_S being the surface salinity flux. Each of these tracer fields is initialized with a uniform value of zero.

2.1.3 ROMS ice model configurations

The ice model used in this study originated in a branch version of ROMS as an implementation by P. Budgell (2005). It is a single category ice model based on thermodynamics by Mellor and Kantha (1989) and elastic-viscous-plastic (EVP) rheology (Hunke & Dukowicz, 1997; Hunke, 2001). A series of modifications of that model were presented and discussed in part 1 of this study, leading to a drastic improvement in the prediction of the ice fraction (concentration) as compared to the satellite data. Here we focus on simulations that use the full set of modifications presented there, both thermodynamic and dynamic. The experiment labelled S_{Dyn} in part 1 forms the basis here but is modified further. In this study the previous S_{Dyn} sea ice model configuration is referred to as $M_{p1\text{-}Dyn}$.

Additional changes were made to the sea ice model in order to more accurately simulate changes in salinity on the Bering Sea shelf. The first alteration was to correct a coding error inherited from the version used as a starting point for part 1. This error caused an overestimate of the salinity flux associated with ice formation in open water portions of grid cells by double-counting a negative surface heat flux as contributing to both surface ice production, w_{ao}, and frazil ice production, w_{fr}. Correcting this error led to more reasonable salinity fluxes in polynya regions (where ice concentration was low, but sea ice production was high). Another modification involved the formulation of the molecular sublayer salinity parameter (S_{ms}) which can have a large influence in the model on ice production and melt rates and on the relationship between these rates and the surface salinity flux. The formulation for S_{ms} in part 1 of this study, which was inherited from earlier ROMS implementations, was found to be inconsistent with that presented in the Mellor and Kantha (1989) paper used as the reference for the ice thermodynamics, but contributed to good predictions of shelf sea ice concentration. Details of the two estimates of S_{ms}, the one in the inherited ROMS code and the one by Mellor and Kantha, are described in Appendix **A**. In sensitivity studies, as described below, we included simulations that utilize the original Mellor and Kantha formulation, referred to as M_{MKorig}.

The most essential change to the sea ice model in this part of the study was replacing the salt flux parameterization with a more conservative form. The original scheme, which is explained in more detail in Appendix A, produced significant net changes in shelf averaged salinity over a seasonal freeze/melt cycle that could not be accounted for by lateral exchanges with the basin or Arctic. Rather the salt flux during a freezing process could differ significantly from the freshwater flux during a comparable melting process. A very simple way to ensure that the brine rejection during freezing equals the freshwater equivalent negative salt flux during melting is to make the salt flux due to ice growth and melt a linear function of the thermodynamic rate of change of ice mass in a grid cell. To this end, we consider a salt flux parametrization in which the difference between surface ocean salinity and sea ice salinity is constant and uniform, as a check on conservation:

$$\boldsymbol{F_S^i} = \frac{\boldsymbol{dh_i}}{\boldsymbol{dt}} \widetilde{\boldsymbol{\Delta S}} \tag{5}$$

where $\widetilde{\boldsymbol{\Delta S}}$ is set to a value close to the difference between the specified sea ice salinity ($\boldsymbol{S_i = 3.2}$) and the shelf-averaged ocean surface salinity ($\widetilde{\boldsymbol{\Delta S}}$=31.5-3.2=28.3). The rate of change of sea ice cell averaged thickness in a grid cell is

$$\frac{\boldsymbol{dh_i}}{\boldsymbol{dt}} = \left[\boldsymbol{c_i}(\boldsymbol{w_{\mathrm{io}}} + \boldsymbol{w_{ai}}) + (\boldsymbol{1} - \boldsymbol{c_i})\boldsymbol{w_{ao}} + \boldsymbol{w_{fr}}\right] \tag{6}$$

where c_i is the ice concentration and the w variables indicate rates of ice production or melt (positive for production) at the ice-ocean ($\boldsymbol{w_{\mathrm{io}}}$), atmosphere-ice ($\boldsymbol{w_{ai}}$) and atmosphere-ocean ($\boldsymbol{w_{ao}}$) interfaces along with frazil ice production($\boldsymbol{w_{fr}}$). Simulations with this salt flux will be referred to as M_{consS} . While this representation is conservative in the sense described above, the brine flux is not proportional to the salinity of the seawater being frozen (while the sea ice salinity in this model is fixed). To allow for this dependence, another scheme is also considered that retains dependence on surface ocean salinity ($\boldsymbol{S_{so}}$), albeit with a possible loss of conservation:

$$\boldsymbol{F_S^i} = \frac{\boldsymbol{dh_i}}{\boldsymbol{dt}} (\boldsymbol{S_{so}} - \boldsymbol{S_i}) \tag{7}$$

This will be referred to as M_{surfS}. This representation is a typical starting point for modern sea ice models that provide much more complex representations of sea ice brine and melt fluxes (Tartinville et al., 2001). In such models, that may focus on longer time scales and more sophisticated sea ice dynamics, ice salinity is often allowed to vary temporally and spatially (both horizontally and vertically) within the ice. Brine rejection may happen over a period of weeks as ice cools. Sea ice flushing and flooding process may be parameterized and evolution of the brine channels may even be considered (Griewank and Notz, 2015; Vancoppenolle et al., 2009). While these processes are all relevant to the Bering Sea seasonal ice, here we continue with the approach of limited complexity. If (5) were used in a model simulation over a closed domain, it would be guaranteed that the domain-averaged salinity before the freezing season is equal to that after all the ice is melted. In contrast, (**7**) could lead to a net change in salinity integrated over a domain, if for example ice formed in fresher water is transported to a region with relatively higher surface salinity to melt. Something like that typically happens on the Bering Sea shelf. Nonetheless, we will find that the model using the M_{surfS} parameterization reproduces shelf salinity observations for the winter of 2009-10 reasonably well (section 3), without deviating significantly from case M_{consS} .

The full surface salinity flux in a grid cell also incorporates evaporation and precipitation. The portion of surface runoff that is associated with melting snow or precipitation is considered freshwater in this model giving the total salt flux in a grid cell as

$$\boldsymbol{F_S} = \boldsymbol{F_S^i} - \boldsymbol{c_i r_{off} S_{so}} + (\boldsymbol{1} - \boldsymbol{c_i})(\dot{\boldsymbol{E}} - \dot{\boldsymbol{P}}) \tag{8}$$

where $\boldsymbol{r_{off}}$ is the rate of surface runoff excluding surface ice melt and $\dot{\boldsymbol{E}}$ and $\dot{\boldsymbol{P}}$ are rates of evaporation and precipitation over the ice-free portion of the grid cell, respectively.

More details on the differences between simulations with $M_{p1\text{-}Dyn}$, M_{MKorig}, M_{consS} and M_{surfS} are presented in Appendix B where the parameterizations are compared in a one-dimensional setting representative of the central Bering Sea Shelf in the winter of 2009-10. This one-dimensional study provides confidence that using a salt flux parameterization such as M_{consS} or M_{surfS} in the full eastern Bering Sea model domain should capture the redistribution of salinity over the winter season due to ice formation without significantly altering the total salt content of the shelf. Comparisons of full model domain solutions using M_{consS} and M_{surfS} with shelf salinity observations below will demonstrate similarly. Despite the differences in the salt flux parameterization between $M_{p1\text{-}Dyn}$ and M_{consS} or M_{surfS}, the new salinity parameterizations did not significantly alter the evolution of the sea ice concentration field in the eastern Bering Sea model compared to the model solutions discussed in part 1 (sect. 2.3), because the formulation for the salinity in the molecular sublayer between ice and ocean S_{ms}, was left unaltered, and effectively decoupled from the ice-to-ocean salt flux estimation. S_{ms} plays a driving role in the melting and freezing processes but can also lead to a loss of salt conservation, depending on how it enters the salt flux parameterization (see Appendix A for the details).

2.2 The global HYCOM benchmark

The ROMS results for salinity and temperature presented here will be compared to results from the global Navy HYCOM solution GLB[u]0.08 (0.08° horizontal resolution) that was mentioned previously with regard to the open boundary conditions. The purpose of this comparison is to illustrate regional shortcomings that this global ocean model product, widely used for oceanographic analyses on multiyear time scales, may present. Although HYCOM includes the option to couple to the multicomponent CICE sea ice model (Elizabeth Hunke et al., 2019), for these publicly available simulations the sea ice is represented through a simpler ‘energy-loan’ model that follows from (Semtner, 1976).HYCOM uses data assimilation to correct sequentially discrepancies between the model state and observations. The data assimilated includes satellite observations of surface ocean temperature and sea surface height, in situ temperature and salinity profiles and satellite estimates of sea ice concentration.

2.3 Satellite data

The simulation results are compared with two satellite products. Primarily, the 5 km-resolution product based on the Arctic Radiation and Turbulence Interaction STudy Sea Ice algorithm (ASI) (Spreen et al., 2008) is used. This algorithm uses the higher frequency (89MHz) channel of the Advanced Microwave Scanning Radiometer to improve spatial resolution at the cost of needing to use weather filters to correct for greater cloud interference in this waveband. While it captures features well it can exhibit rapid fluctuations in ice concentration due to signal interference from clouds. The lower resolution Operational Sea Surface Temperature and Sea Ice Analysis (OSTIA) (Donlon et al., 2012) product, with a nominal resolution of 12.5 km is also used for shelf averaged comparisons. The daily composite ice concentration estimates it provides are based on using data from several Special Sensor Microwave Imager (SSM/I) satellites, processed for EUMETSAT (Andersen et al., 2007). Because OSTIA often over-smooths the concentration fields, it fails to resolve polynyas and so is not considered for model comparison in that portion of this study.

In order to demonstrate the consistency of the ice concentration results in part 1 with those in this part of the study following the changes to the ice model thermodynamics discussed in sect. 2.1.3, Figure 5a from part 1 is replicated here with comparison to the new model solutions (Figure 2). The fraction of the shelf covered in sea ice evolved quite similarly to the earlier results and agreed well with the ASI and OSTIA satellite estimates. This occurs even though the shelf-averaged ice thickness for M_{surfS}, for example, is approximately 0.18m less than for $M_{p1\text{-}Dyn}$ at the winter peak ice extent in mid-March 2010. (The change in ice thickness was largely due to fixing the coding error associated with over-estimating the magnitude of the atmospheric heat flux, mentioned above.)

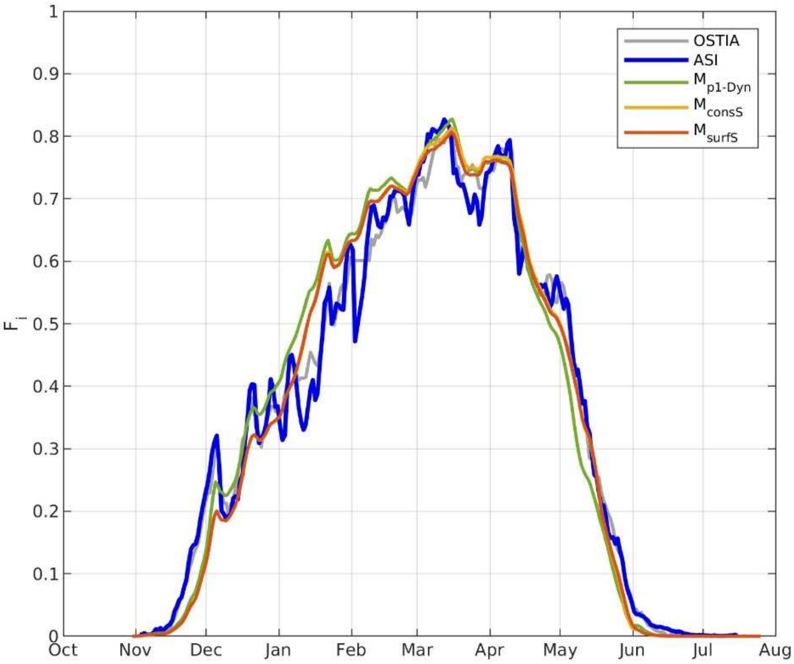

Figure 2. Fraction of the Eastern Bering Sea shelf covered in ice (eq. 16, Part 1) as a function of time for model simulations with ice model modification, the two satellite estimates (OSTIA and ASI) and for a simulation using the ice model as in part 1.

2.4 Field Measurements

As part of the NSF-BEST-BSIERP program a configuration of 9 subsurface moorings were deployed on the central Bering Sea shelf from 2008 through 2010 (2012a) (locations are depicted in Figure 1a). The moorings were arranged in approximately 3 radial lines extending from the Alaskan coast near 61°N, such that there were northern (N), central (C) and southern (S) mooring positions close to the 25m, 40m and 55m isobaths (Figure 1a). The S25 mooring data was not operational during this study period, but we include this location for model-model comparison. Near-bottom salinity data from these moorings were used in this study both for model validation and for the June 2009 initialization of the summer spin-up simulation.

Multi-decadal time series of temperature and salinity are available from moorings that span Bering Strait (Woodgate, 2018; Woodgate et al., 2015). Of the four mooring locations that are examined here, two (A1E and A1W) are in the channel west of the Diomedes, one is in the eastern channel (A2) and one is near the Alaskan coast (A4) (Figure 1b). Near-bottom salinity measurements from these four moorings are used in this study for model validation and analysis. In each case water depth was approximately 50m with instrumentation set 10-20m above bottom. As mentioned in part 1 of this study, current measurements at these same locations were used to adjust the model northern boundary condition to more closely match observed transport out of the Bering Sea. Velocity data will also be used here to help analyze the observed changes in salinity at the mooring locations. The current, temperature and salinity datasets for these moorings are publicly available (Woodgate and Weingartner, 2015; Woodgate, 2011).

From March 7th through April 1 2010 85 CTD profiles were collected from the Coast Guard cutter Polar Sea, covering the region immediately south of St. Lawrence Island and extending out approximately along the 100m isobath past both St. Matthew Island and the Pribilofs (Figure 1c, abbreviated PSEA). This data was also collected as part of the NSF BEST-BSIERP program. Depth averaged temperature and salinity data from this cruise were used here for model validation. This dataset is also publicly available (Stabeno et al., 2011).

3 Model-Observation comparison

In this section, results primarily from the M_{surfS} eastern Bering Sea simulation are compared to both observations and the global HYCOM output. The global HYCOM solution is included in some of these comparisons, not because there is an expectation that it should give comparable results but rather because it is an often referenced, publicly available model output.

3.1 Salinity

Eight of the nine NSF-BEST shelf moorings (all but S25 - Figure 1a) recorded near-bottom salinity time series through the winter of 2010 and have proven useful in describing the spatial and temporal shelf variability (Danielson et al., 2012b). Here, in order to focus on the change in salinity caused by ice formation, comparisons are made at the near-bottom mooring measurement positions (Figure 3). In order to exclude systematic differences in the initial fields, the observations and model outputs are displayed as the salinity difference in each case relative to their time-averaged value for the first week of November 2009 at each mooring position. The water column salinization due to ice formation is most apparent at the northern mooring locations (N55, N40 and N25). Salinity increases earliest and by the greatest amount at the most shoreward mooring locations. The ROMS model captures this pattern well. HYCOM, which drives ice variability in part by assimilation of the ice concentration data, exhibits significantly smaller salinity changes. There is no documentation available to us to suggest that the energy-loan ice model used for these simulations includes a salinity flux parameterization.

Intraseasonal variability in the observations is highest along the central mooring line (C55, C40 and C25). Danielson et al. (2012b) note that salinity on the shelf reaches the annual minimum in late fall, and that the position of the salinity minimum tends to gradually relocate offshore over the course of the winter season, but that that pattern does not hold for the C40 mooring in the winter of 2010. The observations suggest that low salinity water arrives at C40 in mid-November of 2009 but that afterwards the salinity intermittently increases by as much as 2 between February and the first week of April 2010. ROMS displays a similar salinization but without the late fall freshening that appears in the observations. The abrupt changes in salinity at the mooring locations in the model (and presumably in the observations) are due to frontal movements. At times these fronts are associated with freshwater discharge from the Yukon River, strong salinization from nearshore ice formation or a combination of both. In the model, these fronts meander and shift in response to wind events. This likely accounts for the model tendency to produce abrupt changes in salinity at the mooring location that correlate in timing with the observation but not necessarily in magnitude.

Along the southern line of moorings, the M_{surfS} solution overestimates the winter salinity changes at S40, the central mooring. The overestimate may be due to an underestimate of the amount and timing of freshwater input to the shelf over the months preceding the winter that results from using climatological monthly freshwater inflow. This would also explain the model missing lower-salinity signals on the northern two mooring lines between November 2009 and February 2010. Closer to shore, at S25, the ROMS solution shows a winter increase in salinity that is likely reasonable given the proximity of this station to C25 (although no observations are available at S25 for comparison). The global HYCOM solution shows little indication that brine rejection from sea ice formation causes an increase in salinity at any of the mooring locations.

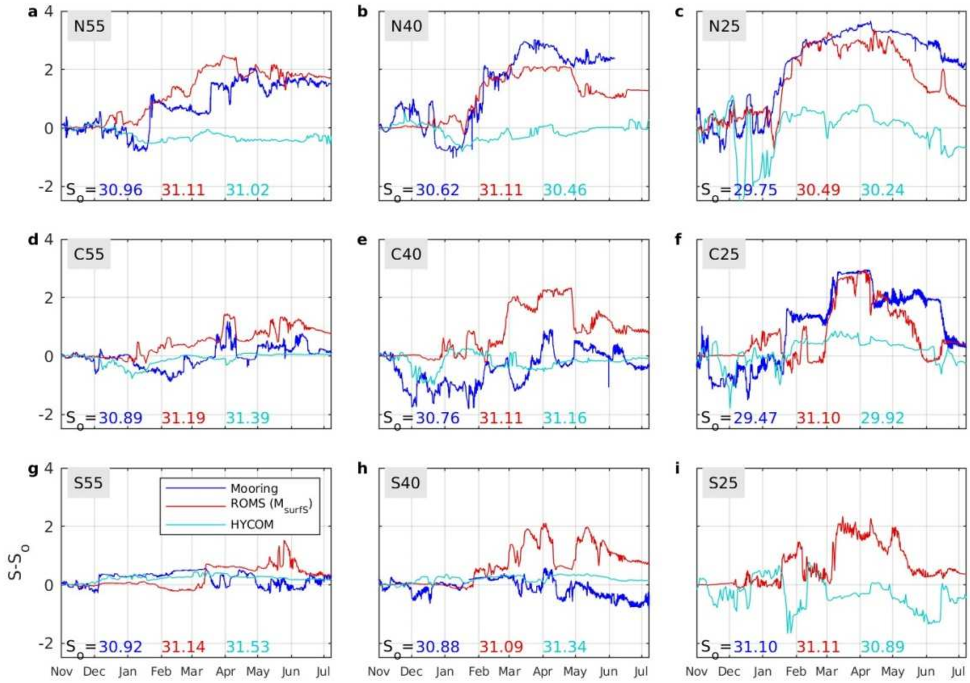

Figure 3 Time series of near-bottom salinity change from initial value (Nov 1, 2009) at the 9 mooring locations on the Bearing Sea Shelf: observations (dark blue), ROMS with M_{surfS} salinity flux parameterization (red), and the global HYCOM (cyan). S_o at the bottom of each plot indicate the initial values.

Salinity observations are also available for the polynya region south of St. Lawrence Island and for midshelf locations roughly along the 100m isobath from the PSEA ship survey that took place in April 2010. Eighty-five profiles of temperature and salinity were collected at locations as depicted in Figure 1c. Figure 4a,b shows the depth averaged salinity and temperature as functions of the distance from St. Lawrence Island (measured from the midpoint of the island southern shore). The figure exhibits the expected pattern of cold salty water under the polynya and warmer fresher water farther offshore where sea ice has begun melting. There is significant variability in both the observations and in the ROMS results in the 200km region closest to the island indicative of the complex flow structure that develops as a result of intermittent brine rejection events. But the change in salinity and temperature as a function of distance from the island in the model is consistent with the observations. As was the case with the mooring data, there is little evidence of salinization of the water column in the HYCOM fields. It is unclear whether this is associated with the rate of ice formation, the salt flux parameterization or a failure of the model to resolve the polynya dynamics (sea ice fields from HYCOM were not available for analysis).

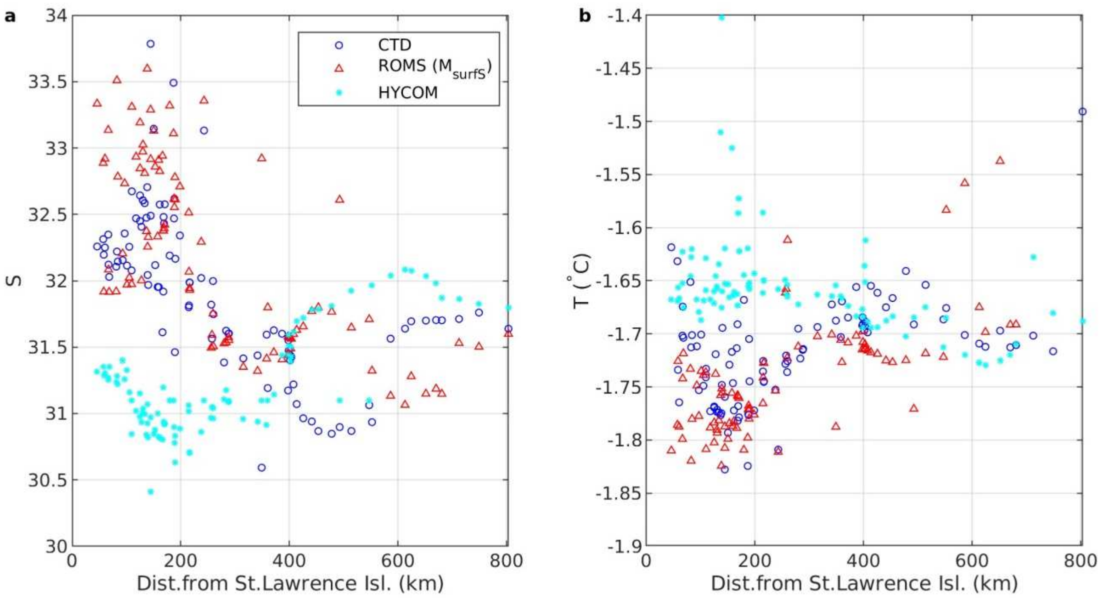

Figure 4 Depth-averaged (a) S and (b) T at the PSEA CTD locations as a function of distance from St.Lawrence Island (see Figure 1c). Observations (blue circles) are compared with ROMS- M_{surfS} (red triangles) and HYCOM (cyan dots).

Salinity and velocity data from the Bering Strait moorings (Woodgate, 2018; Woodgate et al., 2015) (Figure 1b) provide information on the exchange with the Arctic. When flow is northward, out of the Bering Sea, the water passing the western mooring locations (A1E and A1W) typically have characteristics of Anadyr current water and the shelf waters along the Chukotka coast (Figure 5). The water characteristics at the eastern moorings (A2 and A4) during northward transport resemble those of the eastern Bering Sea inner shelf and the Alaska coastal current (Woodgate et al., 2015).

Variability in the salinity at the two western moorings (A1W and A1E) is less than +/-1 between January and July 2010 when the current through the strait is predominantly northward (Figure 5a and b). This low variability is in part due to the outflow of Anadyr current waters that have origins at the shelf break where ice formation is limited and that transit the shelf relatively quickly. The ROMS and HYCOM model results are consistent with this in general. When the transport is southward through the straight (November through early December 2009) the data from A1W and A1E moorings show significant freshening of the water column. This feature depends on transport of fresher water from the Arctic. It is not captured in the ROMS solution in part due to an underestimate of the southward transport (based on velocity comparison at the mooring locations during this period) and in part due to a lack of a fresher water source from the north. It may be that early-season ice is advecting out of the Arctic during this period and melting in the vicinity of the strait.

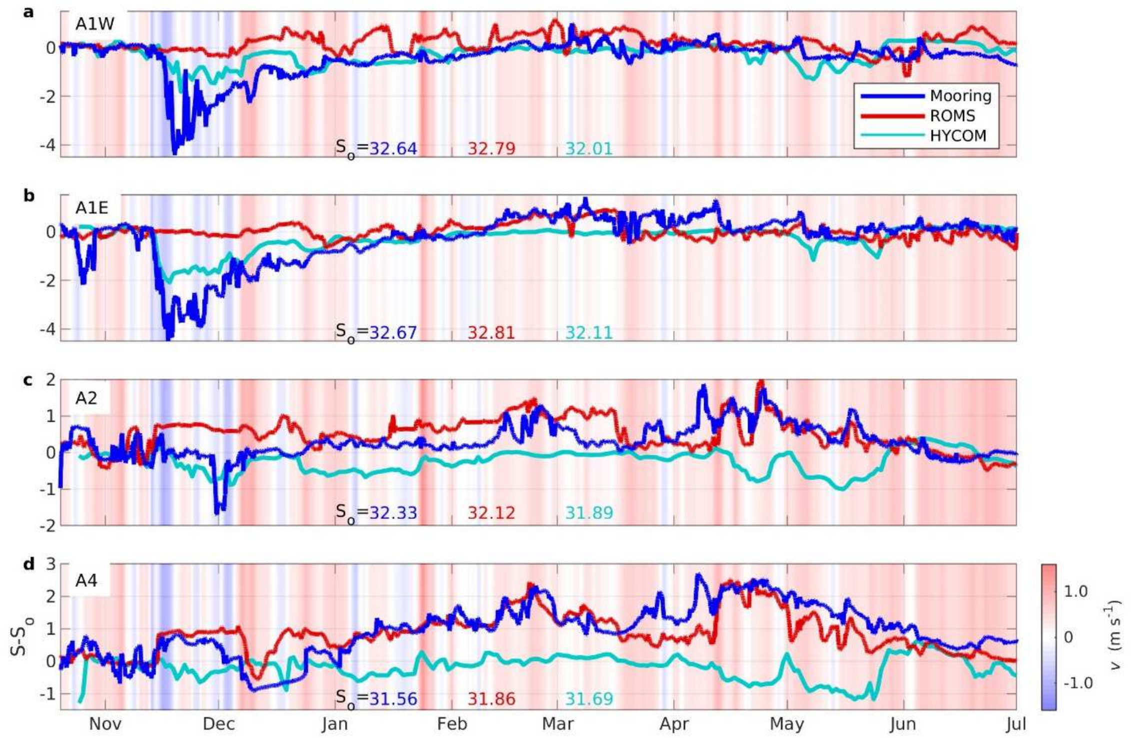

Figure 5. Near-bottom salinity change for models and observations at the 4 mooring locations located in the Bering Strait. Background shading indicates northward current velocity from the mooring data. S_o is the time averaged salinity over the first week of November in each case.

Variability in salinity between January and June 2010 is relatively larger east of the Diomedes, at the eastern mooring locations A2 and A4 (Figure 5c, d). Positive fluctuations during periods of strong northward transport such as in late February 2010 and mid-April 2010 are associated with northward transport of saltier water from the northern Bering Sea shelf, primarily east of St. Lawrence Island. These peaks in salinity are likely associated with northward flow of water from regions of high sea ice production. As mentioned above in discussing salinity comparison at other sites, the ROMS simulation captures salinization of the water column by sea ice formation more accurately than the global HYCOM solution on the northern Bering Sea shelf. This may explain the better match with observations of the ROMS solution at A2 and A4.

3.2 Ice concentration

In part 1 of this study, comparisons were made between the model ice concentration and satellite estimates. Results were presented that demonstrated the model skill in capturing the overall advance and retreat of sea ice as well as the appearance of the St. Lawrence polynya. In order to further analyze the model skill in capturing polynyas, the full season of ASI daily satellite-based estimates of ice concentration (Spreen et al., 2008) is examined and additional coastal regions with intermittent reductions in c_i are identified during the winter of 2010. These include (Figure 6a): (1) the southern side of St. Lawrence Island, (2) the southern end of the Chukotka Peninsula, (3) the southwestern-facing portion of the Seward Peninsula, (4) the eastern-facing Alaskan coast in the vicinity of Unalakleet

(Norton Sound), and (5) the northwestward-facing Alaskan coast region near the Yukon river outflow. The open water fraction is defined as in part 1:

$$\boldsymbol{O_w} = \frac{\boldsymbol{1}}{\boldsymbol{A_{reg}}} \sum_{\boldsymbol{j=1}}^{\boldsymbol{N_{reg}}} (\boldsymbol{1} - \boldsymbol{c_j}(\boldsymbol{t}))\Delta\boldsymbol{x}\Delta\boldsymbol{y} \tag{9}$$

where A_{reg} is the total area of the region. The model estimate of open water fraction on average exceeds the satellite estimate for the northeastern Bering Sea shelf overall (Figure 6g) and for most of the five small regions (Figure 6b-e), but the discrepancy is generally small. Early in the season the model tends to underestimate ice coverage likely due to a warm bias in SST. But throughout much of the winter, changes in ice concentration in the model, in the polynya regions, are well correlated with the satellite observations. In some cases, rapid change in satellite estimates of O_w may reflect limitations of the processing algorithm, as consecutive daily composites exhibit differences that appear to occur more rapidly than can be accounted for by sea ice advection or surface heat loss. The model tends to show more persistent periods of high O_w than the satellite in most regions (Figure 6b, c, d, e). It is conceivable that after polynyas form, cloud formation over the open water may be misclassified as ice, reducing the observation based O_w prematurely.

Landfast or grounded sea ice plays a role in some of the discrepancies in O_w between the model and observation along the Alaskan coast. Satellite imagery indicates that grounded sea ice persists along portions of the Alaskan coast for up to 2 weeks at a time, esp. in March and April of 2010 (Figure 7a; a supplemental animation showing the distribution of ice concentration from the model and from the satellite estimate is included to demonstrate the persistence of this feature: Sea ice concentration model-satellite comparison). Polynyas only develop at the offshore edges of these features, consequently, reducing O_w in the Alaskan nearshore region. The model however does not include a mechanism to account for grounding or landfast ice. As a result, the modeled polynya opens up right at the coast (Figure 7b). Consistently, the model estimates of O_w exceed the satellite estimates in these regions (Figure 6e,f) when landfast ice is present.

The model underestimates O_w in January and February in the Yukon delta region (region 5; Figure 6f), for a related reason. Close examination of the satellite derived ice concentration fields in this area shows that a promontory of grounded or landfast ice at times extends offshore in the vicinity of the river delta (Figure 7c), blocking the transport of ice from the northeast into this region. Several times during these months when winds shift to north-northeasterly, the promontory of landfast ice blocks southward transport of sea ice leaving a band of ice-free water along the coast in the shadow of the promontory. Lacking the ice promontory, sea ice quickly covers this polynya region in the model (Figure 7d), leading to underestimates of O_w (Figure 6f).

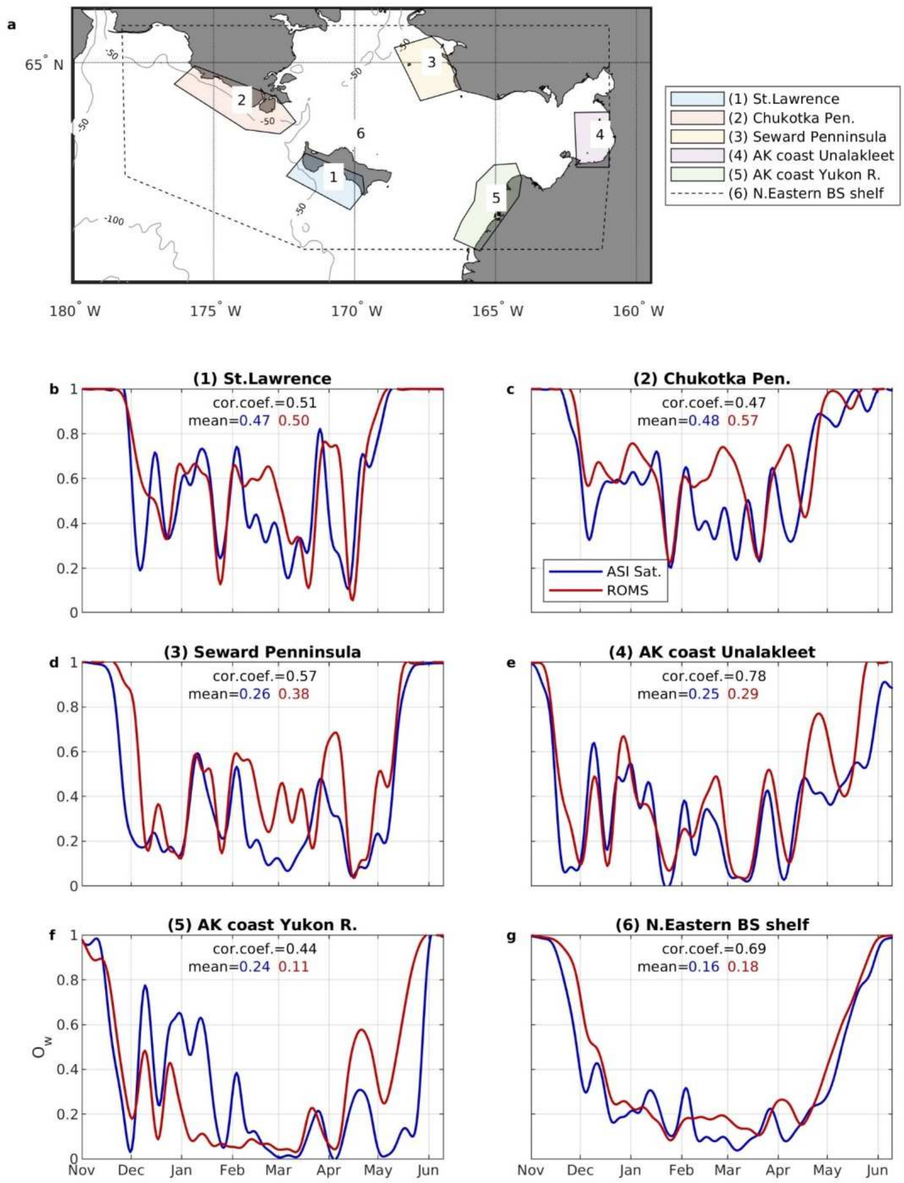

Figure 6. Comparison between model and satellite estimate of open water percentage as a function of time for the 6 regions delineated in the map in panel **a** *. Model-observation correlations and time means, calculated using the time series between December 1 2009 and May 1 2010, are noted on each plot. Fields are low pass filtered (~ 5-day).* .

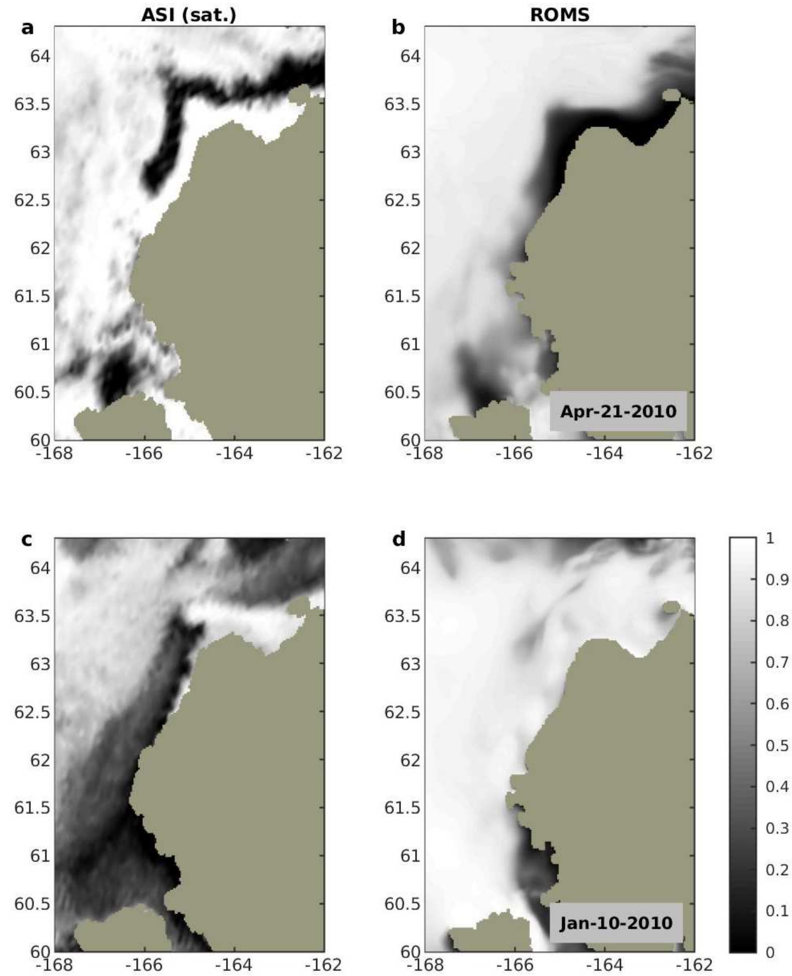

Figure 7. Ice concentration from satellite (a,c) and model (b,d) estimates in the vicinity of the Yukon river delta. On the two days displayed, landfast ice is present in the observation but not the model results. In (a), the polynya opens up offshore of the landfast ice; in contrast, in model (see b) the polynya opens next to the coast. In (c), it is apparent that the landfast ice north of 63N blocks southward transport of ice protecting the coast south of 63N. The model (see d) does not include the landfast ice mechanism and lets ice from the north fill the coastal area.

The appearance of polynyas in the Bering Sea coastal regions is typically correlated with winds. In order to examine the relationship between wind direction and enhanced open water area in each of the regions delineated in Figure 6a, polar histograms are generated (Figure 8). Each histogram shows counts of 3 hour-averaged model forcing winds greater than 3 m/s between December 1 2009 and April 15th 2010 sorted into directional bins (gray bars). Blue bars count how often O_w based on the satellite estimate is greater than the December-April average for the wind events in each bar segment. Note for this analysis the O_w estimates are sampled with a 24-hour time lag. Likewise, red bars count occurrences of greater than average O_w based on the model for those wind events.

Over the winter, winds are predominantly to the south-southwest over much of the Bering Sea shelf (Figure 8). Consequently, coastlines perpendicular to this orientation such as the south side of St.

Lawrence Island and the Chukotka peninsula have the highest count of larger than average open water area (Figure 6b,c). For both these regions, the observations and the model consistently produce higher than average O_w with greater than 3m/s winds in these directions. This is indicated in Figure 8a and b, by the nearly identical size of the blue and red bars that are no shorter than the gray bars for each wind orientation. Along the Seward peninsula (area 3 in Fig. 6a), there are numerous occurrences of above average O_w associated with southward winds (Figure 8c) despite this coastline being aligned primarily west-southwest. This appears in both the observations and the model. Presumably the enhanced open water results due to blocking of sea ice transport by the Bering Strait promontory just to the north of area 3 (see Figure 6a).

There are notable differences between the modeled and observed response to winds along the regions of the Alaskan coast near Unalakleet and the Yukon river (areas 4 an 5 in Fig. 6a; Figure 8d,e). The reason for the discrepancies near the Yukon river mouth relate to the formation of a landfast ice promontory at the northern end of this region as discussed above and depicted in Figure 7c. The differences in the Unalakleet region also result from inaccurate representation of the sea ice physics nearshore. The occasions when the model exhibits greater than average O_w but the observations do not are mostly associated with south-southwestward winds. During these periods, the model allows the sea ice to be ‘flushed-out’ to the west, but the satellite imagery suggests it accumulates becoming landfast along the northward-facing coast between areas 4 and 5.

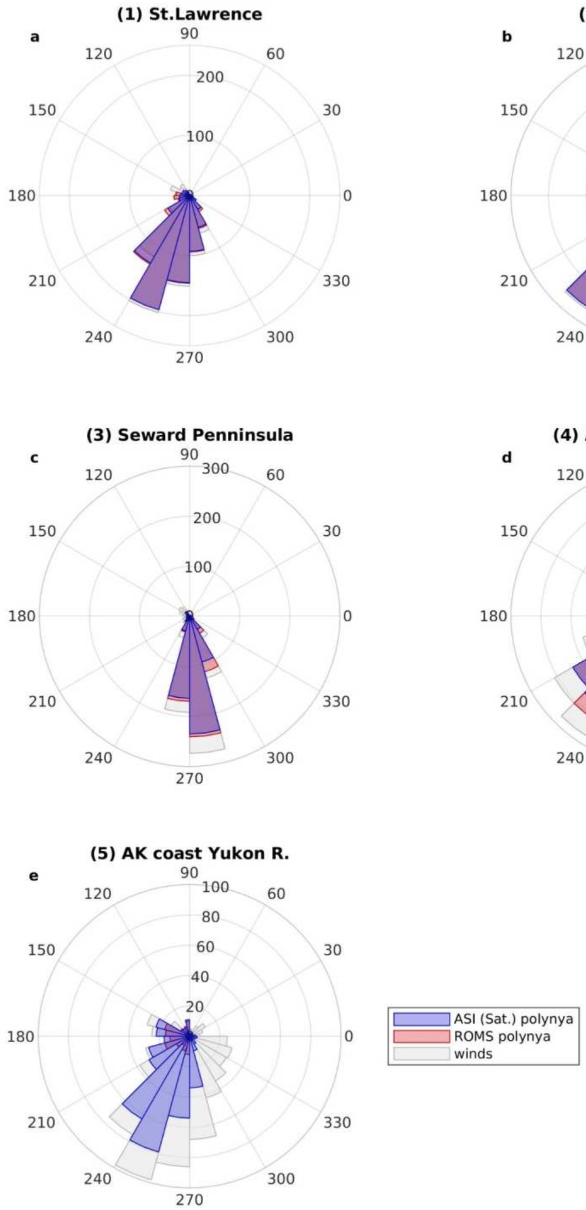

Figure 8. Polar histograms showing the distribution of 3-hourly average wind direction from the NARR model in each of the regions depicted on the map in Figure 6a between December 1,2009 and April 15th, 2010 (gray). The semitransparent blue and red bars denote times when the open water area in each of the regions was higher than the seasonal northern shelf averaged (Figure 6g) based on the satellite estimate and the model respectively. A time-lag of one day was used when associating wind direction with open water area.

4 Oceanic variability over the Bering Sea shelf in winter

4.1 Redistribution of shelf salinity

The efforts to arrive at a reasonably accurate representation of the ice-ocean salt flux were made here in order to make an accurate assessment of the overall salinity changes on the Bering Sea shelf in winter. Numerical models, with some demonstrated fidelity for matching observations, are uniquely qualified for such analysis due to the spatial and temporal extent of the information they can provide. For the Bering Sea shelf several competing fluxes determine the overall salinity changes. These include the brine/melt cycle associated with sea ice formation, the exchange of water and ice with the Arctic and Bering Sea basin, freshwater riverine inflows (particularly in late spring) and precipitation and evaporation. In relatively cold winters, including the winter of 2009-10, the factor that likely leads to the largest changes in shelf averaged salinity is ice formation and melt, so accurate representation of this component is essential for a meaningful analysis of how salinity is redistributed over the winter.

In the simulations conducted for this study the estimates of the seasonal change in shelf averaged salinity (shoreward from the 200m isobath) between November 2009 and June 2010 differ notably depending on the salt flux parameterization used (Figure 9a). With both M_{consS} and M_{surfS}, the shelf-average salinity returns by the end of winter nearly to the same value it had at the start of the season. Of course, when open boundaries are present, even with a conservative scheme such as M_{consS}, the overall dilution due to melt will not match the brine added during ice formation if ice enters or exits the domain in unequal amounts. So, this result suggests that if there were net import or export of ice in the winter of 2009-10, the effect on salinity was compensated for by a comparable lateral exchange of salt. The similarity in the curves for the M_{consS} and M_{surfS} cases further suggests that the net effect of sea surface salinity variations on the overall salt flux was not large.

Other simulations ($M_{p1\text{-}Dyn}$, M_{MKorig} and in the HYCOM solution) showed notable changes in shelf averaged salinity over the winter season (Figure 9a). For $M_{p1\text{-}Dyn}$ and M_{MKorig} these changes cannot be attributed to boundary flux differences because the circulation and ice volumes were similar across all the ROMS simulations. So they are necessarily related to the surface salinity flux differences. There is a net positive change over the season with M_{MKorig}, similar to the one-dimensional experiment in Appendix B. $M_{p1\text{-}Dyn}$ also exhibits a net positive salinity change here. As mentioned earlier it was this overestimate in shelf salinities compared with observations that led to considering the M_{consS} and M_{surfS} formulations.

The global HYCOM solution exhibits a shelf averaged decrease in salinity over the winter (Figure 9a) suggesting that the model may underestimate brine rejection and/or over-dilute the shelf during ice melt. It may also have notably different lateral boundary salinity fluxes compared to ROMS, e.g., across the 200-m isobath. In the HYCOM solution there is no distinction between the pattern in average salinity on the outer shelf (between the 75m and 200m depth contours) and the inner shelf (inshore of the 75m isobath) (Figure 9 b and c). In both subdomains the HYCOM average salinity increases during freeze-up, between November and April, and decreases during melt afterwards. This is not the case for any of the ROMS simulations, for which much of the ice production occurs on the inner shelf leading to a strong local increase in salinity during freeze-up (Figure 9c). In contrast, on the outer shelf in the ROMS solutions, where there is less local ice production but significant influx of sea ice that subsequently melts, there is net freshening throughout much of the winter (Figure 9b). In all ROMS cases, the inner shelf finishes the winter season saltier than it began and the outer shelf becomes fresher. While lateral fluxes contribute in both cases, the primary driver is the net amount of sea ice formation and melt occurring locally.

The effect of including surface salinity in the salt flux parameterization can be compared by looking at the small differences between the M_{consS} and M_{surfS} solutions. In the M_{consS} case the rate of salinization or freshening is solely a function of the rate of ice production or melt. While this allows the scheme to be conservative over a closed volume, the tendency (given the choice of the coefficient in Equation **5**) is to withdraw more salt than M_{surfS} during melting, where the surface salinity is greater than 31.5 and to add more salt than M_{surfS} during freezing where the salinity is less than 31.5. Since the surface salinity is generally greater than 31.5 offshore of the 75m isobath, M_{consS} freshens offshore waters more than M_{surfS} as depicted in Figure 9b, though the effect is small. As the M_{surfS} solution most accurately balances the objective of salt conservation with accurate representation of local changes in salinity, it will be used exclusively in the model analysis that follows.

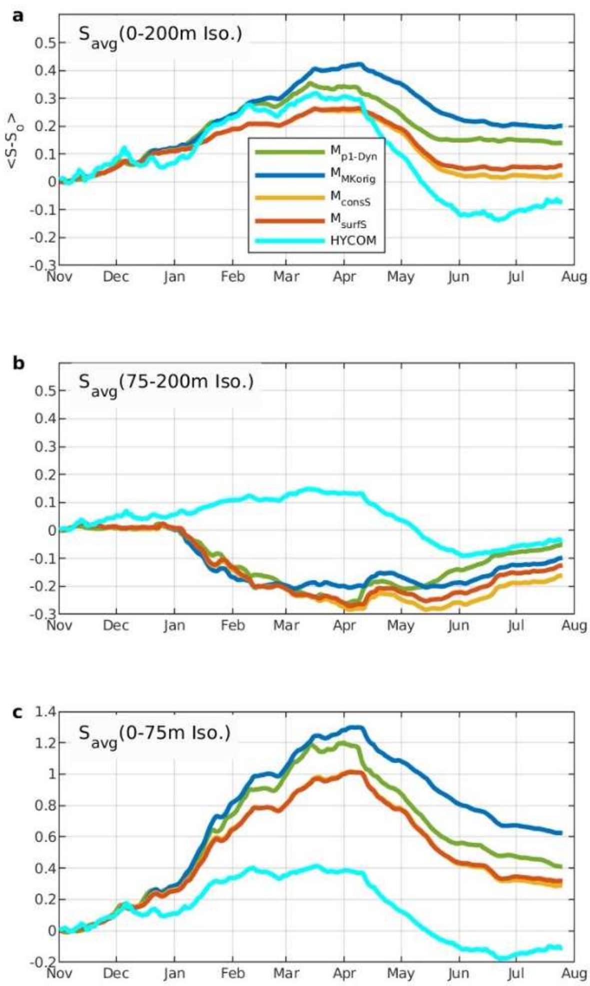

Figure 9. Shelf averaged salinity change since Nov.1 2009 for 4 model cases and HYCOM. **a** *for the full shelf, averaged between the coast and the 200m isobath.* **b** *for the outer shelf, averaged between the 75m and 200m isobath* **c** *for the inner shelf, averaged between the coast and the 75m isobath.*

Figure 10 displays a map of the depth averaged salinity distribution on the shelf at the onset of the winter season (November 1, 2009, panel a), at the time of maximum sea ice extent (April 10th, 2010, panel b), and once all the sea ice on the shelf has melted (July 1, 2010, panel c). (A link is provided to an animation of bottom salinity to elaborate on what is displayed in this figure: bottom salinity animation.)

Before the winter season, the salinity pattern is dominated by the effect of freshwater input primarily from the Yukon River (in the east) and saline water transport between the Bering Sea slope and the Bering Strait via the Anadyr current (in the west). By the time of maximum ice extent in early April, the shallow coastal regions exhibit the highest salinity on the shelf, while the mid-shelf persists with the lowest depth averaged salinity. The dividing line between regions of net salinity increase and reduction lies roughly along the 75m isobath (Figure 10 e and f) and remains at this position throughout the season of ice retreat. The outer shelf ends the season with an average salinity decrease of approximately 0.1, while the inner shelf ends up approximately 0.3 saltier (Figure 9 b, c).

The high salinity of the waters along the Eastern Bering Sea coastlines result in part from local ice formation but also reflect the typically north-to-south circulation near the shorelines. In particular, saltier water from strong brine rejection along the coast of the Seward Peninsula circulates southward along the Alaskan coast as far south as the Kuskokwim River in the model (see Fig. 10e). Similarly, saltier water produced in the model in Kresta Bay on the Chukotka Peninsula (near 179W, 66N), advects southward past Anadyr Bay.

Averaged over the winter, currents close to the surface (Figure 11a) are strongly influenced by the direction of winds and sea ice movement. But at mid-depth and lower (Figure 11b, c and d) an overall anticyclonic circulation can be recognized through much of the winter, driven by the Bering Slope current on the outer shelf, and the Anadyr current on the northwestern shelf. In the model, this pattern eventually leads to some of the mid-shelf meltwater advecting back north in Anadyr Basin towards the high salinity coastal regions of the northern inner shelf.

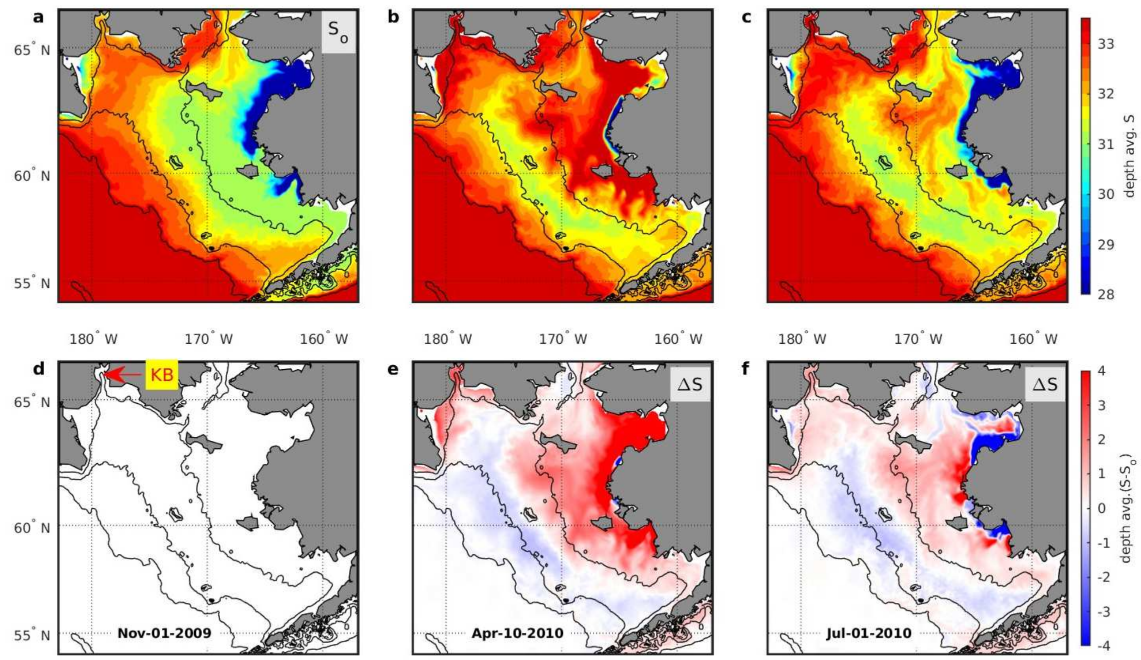

Figure 10. **a** *The depth averaged salinity distribution on Nov.1 2009,* **b** *April 10th, 2010 (peak ice extent) and* **c** *July 1,2010 from the M_{surfS} simulation. Lower panels show the difference in depth averaged salinity for these dates, from the initial distribution displayed in panel* **a**. *Bathymetric contours are for the 200, 100 and 50m isobaths. Acronym KB denotes Kresta Bay.*

The simulations show southward flow from the surface through mid-depth in Shpanberg Strait (between the east side of St. Lawrence Island and the Alaskan coastline). Clement et al (2005)reported, in a modeling study of interannual variability in transport on the Bering Sea shelf, that typically this flow is northward, but tended to shift southward in years, in which winds were predominantly from the east rather than the north. The winter of 2009-10 exhibited mostly northeasterly winds perhaps supporting the correlation they observed and the possibility that this winter differed in a notable way from the historical average. Danielson et al.(2012a) noted from current meter observations between July 2008 and July 2010, that depth averaged transports in Shpanberg Strait were southward when winds were northwesterly, in agreement with our modeling results. They also examined model simulations for earlier years, identifying December of 1999 as exhibiting similar circulation. Clement et al. noted reversal in their model as well during the same period.

The complex spatial distributions of brine and melt water that develop during winter due to the variable weather and the intermittency of polynyas can be analyzed using the passive tracers (2)-(4). These represent the contributions of the positive and negative components of the surface salinity flux and the net surface salinity flux. Depth integrals of these fields are displayed in Figure 12 (a supplemental animation of these fields overlaid with atmospheric wind forcing and sea ice concentration has been included as a supplement: Depth integrated brine and melt tracer animation .

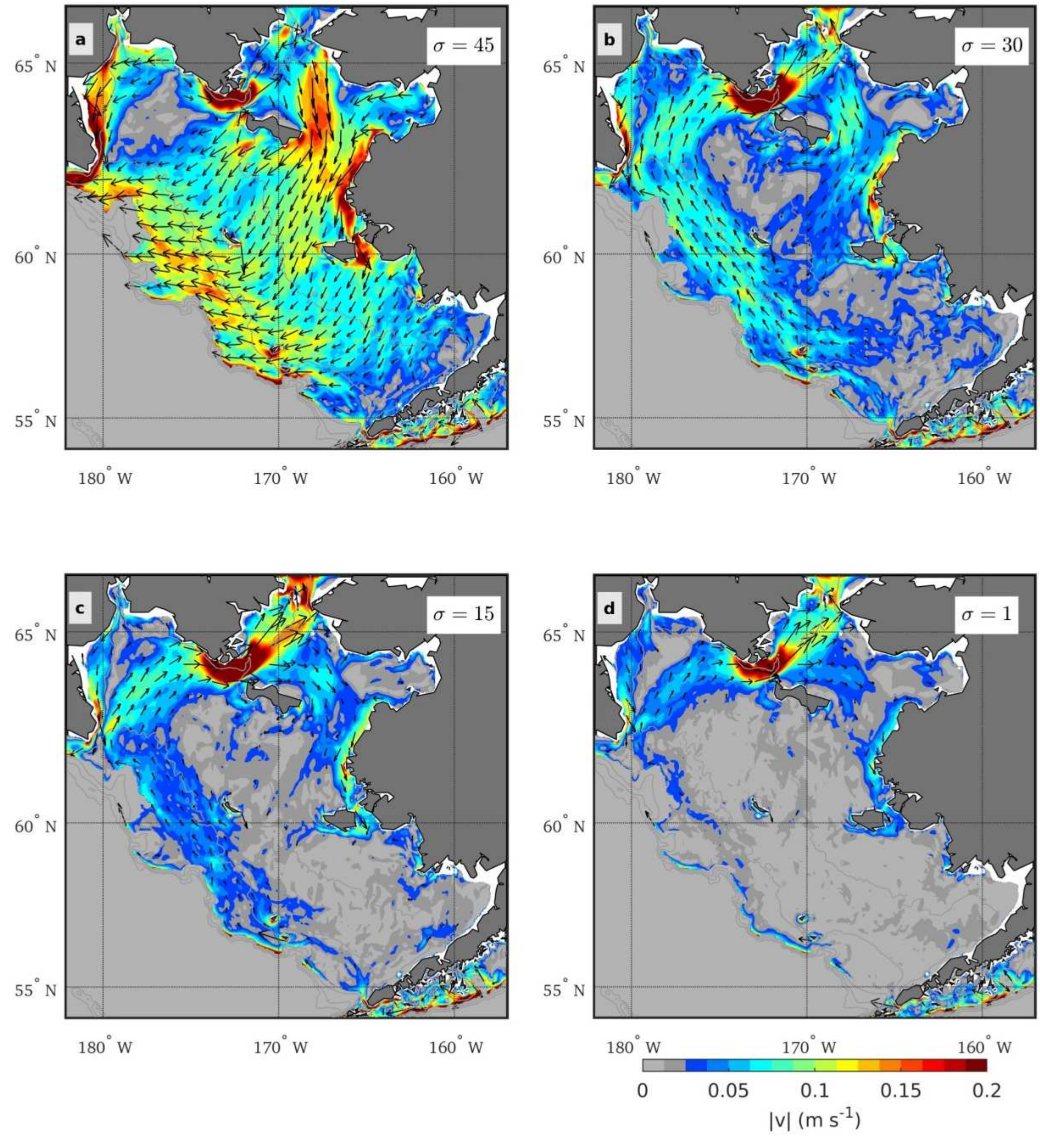

Figure 11. Winter-averaged (Dec 2009-Apr 2010) velocity vectors with color indicating velocity magnitude, for four model levels between the near-surface (σ=45) and the near-bottom (σ =1).

These fields allow us to easily identify regions where the highest brine concentration waters or the most meltwater accumulate and where they form. For example there is very high brine concentration water south of Nunivak Island (60N) inshore of the 50m isobath that originates farther north from along the Alaskan coastal region near the Yukon river outflow (Figure 12d). As the water advects southward it increases in salinity until it reaches warmer (and potentially saltier) surface waters where melt exceeds ice formation (Figure 12 f,i). This occurs in the model approximately 100km shoreward of the ice edge by late March. The brine water produced in the St. Lawrence polynya region (63N) similarly at times advects south and at other times westward but accumulates primarily in the region between St. Lawrence and St. Matthew islands. Kresta Bay is a region of high brine production as well. Waters from Kresta Bay flow south along the Russian coastline through most of the winter, occasionally being entrained into the Anadyr Current. Late in the season however, strong inflow into the domain along the Russian coast flushes the coastal region south of Kresta Bay causing the accumulated brine water displacement to the east of the bay along the southward facing portion of the Chukotka peninsula, before entraining into the Anadyr current (Figure 12g,j). One region where brine accumulates close to where it initially fluxed into the water column is in the vicinity of Nome, along the southern coastline of the Seward Peninsula in Norton Sound. This portion of the Alaskan coast does not appear to flush brine water as effectively as portions of the coast (Figure 11) to the south, perhaps due to its geography. Meltwater accumulated primarily on the mid- to outer shelf (between the 50 and 200m isobaths) through April of 2010 (Figure 12, middle column). Some of the outer shelf meltwater recirculates north of St Lawrence Island carried by the Anadyr current, while some is entrained off the shelf into eddies of the Bering Slope current (Figure 12k). By late April, there is melting inshore of the 50m isobath as well.

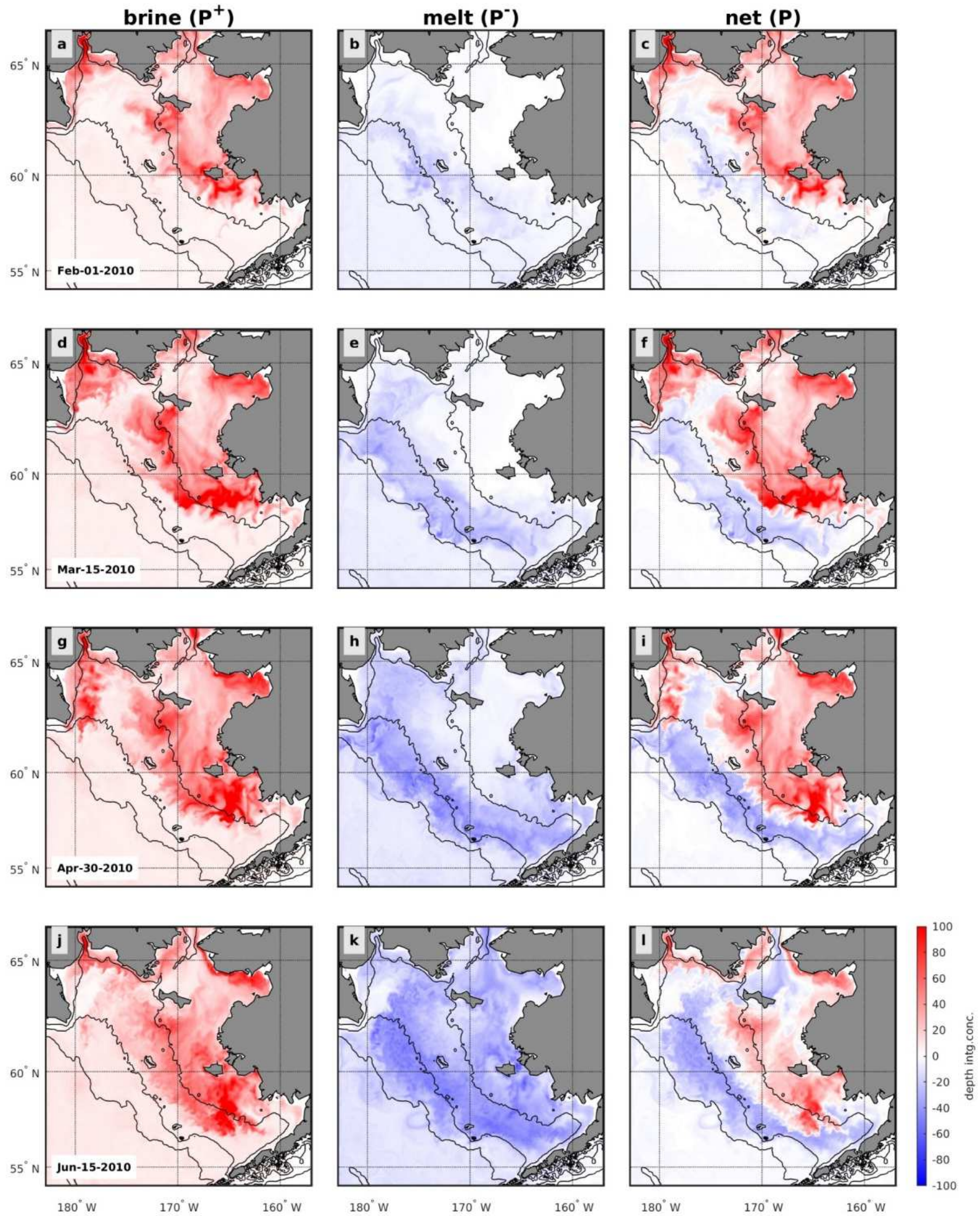

Figure 12. Depth integrated brine flux tracer (2) (left column), meltwater flux tracer (3) (center column) and net tracer (4) (right column) on four selected days from the M_{surfS} case.

While the surface salt flux tracer analysis identifies how brine and meltwater are distributed on the shelf, it can also provide insight into how the preexisting fall shelf salinity distribution was rearranged over the winter. By subtracting the salt flux tracer (P) from the model salinity field (S'=S-P) it is possible to explore how circulation and boundary fluxes alone redistribute salinity over the winter season. In particular, we can examine how the low salinity nearshore water that results from the Yukon and Kuskokwim river outflows is advected and stirred laterally. *Figure 13* displays S' at four different times over the season (a supplemental animation has also been included to aid in the visualization: S' animation for bottom model layer). In mid-December (Fig. 12 a) the distribution appears quite similar to the initial state (Figure 10a), with fresher water hugging the coast from Norton Sound to the Kuskokwim outflow. But a strong inflow of saltier Arctic water tends to flush much of this fresher water southward to the vicinity of Nunivak island by the beginning of February 2010 (*Figure 13*b) and farther south by mid-March (*Figure 13*c). Thus the increased salinity apparent onshore of the 50m isobath in the eastern Bering sea in Figure 10f results from the combined effects of ice formation and the Arctic saline water influx. The low S' water that is pushed southward (and some also eastward into Norton Sound), which was the freshest on the shelf at the start of the season, has experienced some of the strongest brine injection of any water on the shelf (Figure 12d). As this water advects and stirs laterally, in portions, it increases in density due to ice formation, while other portions may decrease due to meltwater freshening. The resultant filamentous patch of low S' water visible to the south of Nunivak island in panels c and d of *Figure 13* results from a complex evolving circulation as horizontal density gradients are altered by the lateral and surface processes (apparent in the animation).

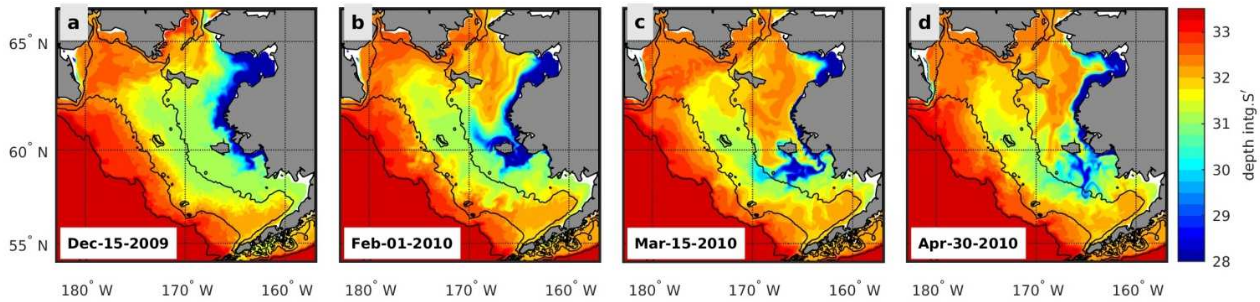

Figure 13. Evolution of the depth integrated salinity field (S') excluding surface fluxes with sea ice and atmosphere.

4.2 Circulation of the sea ice

Transport of the seasonal sea ice that lies atop the coastal waters of the Bering Sea shelf is driven primarily by winds but also by the ocean currents. The ice age tracer (1) is a convenient tool for tracking how sea ice moves over the course of the winter, as much of the earliest ice is produced at the northernmost latitudes of the domain along coastlines, or is advected into the domain through the Bering Strait. In our implementation, the no-gradient boundary condition is used for the ice at the northern boundary (in Chukchi Sea). Since no information about the ice age is obtained for this ice, some of which will later be advected in the Bering Sea through the Bering Strait, all ice advecting into the domain through the Bering Strait is assumed to have formed on November 1, 2009 (recall this was the intial date for the series of the coupled tests presented here). Figure 14 displays maps of ice age at six times over the winter season (a supplemental animation has been included: Ice age animation). Throughout the winter the average age of ice tends to be lowest in regions of active ice formation and export (such as polynyas). Ice ages as it is transported generally southward to the outer shelf. While new ice formation can only reduce the average age of a parcel of ice, ice transported to the warmer waters of the outer shelf ages steadily. As a result, some of the oldest ice accumulates at the ice edge. This is consistent with the established idea of a sea ice 'conveyor belt' from north to south in the Bering Sea (Pease, 1980). The pattern in Figure 14 (c,d and e) indicates northwestward advection of this surviving ice along the shelf break, with the slope current. The anticyclonic circulation is nearly closed when some of this old ice is transported northward with the Anadyr Current. Late in the season, as the ice edge retreats from the shelf break, the alongslope transport of the ice is terminated. The oldest remaining ice appears to be that advected in through the Bering Strait much earlier in the season and accumulated in the vicinity of Nunivak Island (Figure 14f).

The apparent influx of Arctic sea ice (indicated by the oldest seasonal ice) is one of the most prominent features in the ice age distribution. In general winter influx of sea ice from the Arctic has been thought to be low except for in anomalous years (Babb et al., 2013). But based on their analysis of satellite derived ice drift velocity in the Chuchki Sea in the vicinity of Bering Strait, Babb et al. (2013) quantify winter 2009-10 as the season with the second strongest seasonal average southward transport in that region over the 33 years of data analyzed. So, the presence of an influx in the model is not surprising. The pattern can also be interpreted as demonstrating the distribution of the longest surviving ice, which is likely to originate in the northernmost extreme of the model domain.

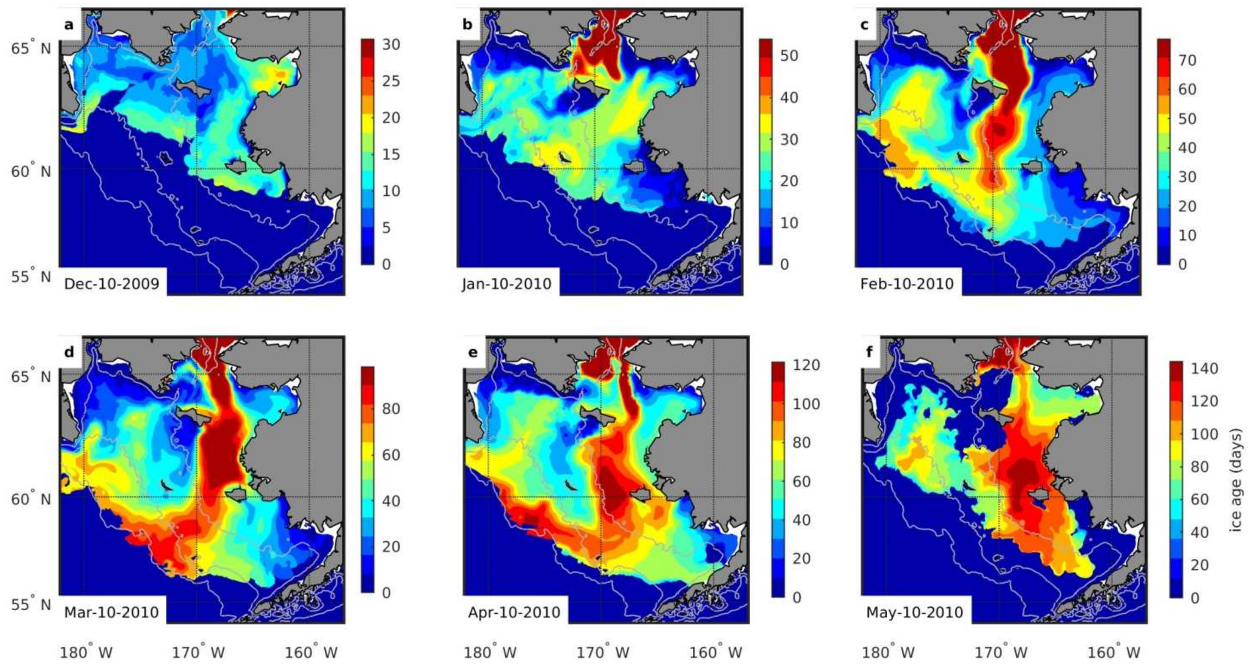

Figure 14. Monthly snapshots of Ice-age for the M_{surfS} simulation.

4.3 Comparison of polynya regions

As demonstrated in Figure 8, polynyas on the Bering Sea shelf tend to be associated with offshore winds. They are regions of enhanced sea ice production and brine injection. So, they play an important role in determining how shelf salinity changes over the winter season. Satellite based measurements now provide reasonably accurate estimates of the changes in open water area associated with these features but cannot yet provide accurate information about their ice production rates nor the potentially differing dynamics and thermodynamics that lead to their formation.

In Section 3.2, the modeled ice concentration was compared to satellite estimates for the 5 polynya regions (depicted in Figure 6a). Figure 14 provides additional time series information on these 5 regions quantifying their relative contributions to the sea ice-ocean salt flux. The cumulative salt flux per unit area, S_f, and the cumulative ice production per unit area, m_i, are shown in Figure 15a. Each of these regions produced ice (on a per unit area basis) at a higher rate than the northern shelf average (also depicted in Figure 15a). The rate of productivity in the St. Lawrence polynya region was the highest, followed by the Seward peninsula region, the Chukotka region, and the two Alaskan coastal regions. In all the regions displayed in the figure, more ice was produced than eventually melted indicating that there was a net export of ice from each. S_f for each of these regions followed the same pattern as m_i, as is expected with this salt flux parameterization. Ice formation in fresher water leads to less salt flux. Consequently, regions such as the Alaskan coast near the Yukon outflow exhibit lower rates of salt flux relative to ice production early in the winter.

An interesting difference that emerges from this analysis is that the Chukotka peninsula box exhibits stronger negative heat flux than either the St. Lawrence or Seward Peninsula boxes yet produces less ice and fluxes less salt per unit area. Polynyas can be classified as predominantly latent or sensible heat polynyas. Latent heat polynyas arise when the mechanical action of the wind sweeps sea ice out of a region exposing freezing temperature water that rapidly begins to produce new ice (the phase change being a latent heat process). Sensible heat polynyas on the other hand exist where surface waters exceed the freezing temperature, allowing for the persistence of open water despite a strong heat flux to the atmosphere (the exchange with the atmosphere primarily alters the temperature but not the phase of the surface water, a sensible heat process). The Chukotka coastal region has a larger negative net surface heat flux (out of the ocean) per unit area than any of the other regions (Figure 15b) in part because this region stays more open (has smaller ice concentration) throughout the season than the other regions (Figure 6). But the associated salt flux falls below that of the St. Lawrence or Seward regions because this portion of the Chukotka coast has some characteristics of a sensible heat polynya. Intermittently, throughout the winter the model predicts the Chukotka region to exhibit above-freezing surface temperatures (Figure 15d), which reduce brine rejection and ice formation. This does not indicate that the Chukotka coast polynya should be classified as an entirely sensible heat polynya however, as it presents characteristics of latent heat polynyas as well. With a coastline roughly parallel to the south coast of St. Lawrence Island, it experiences comparable winds and events of open water coincide with winds to the southwest (see Figure 8). So the presence of the warm water alone did not produce polynyas off the Chukotka coast in the winter of 2009-10, but rather inhibited ice formation when the polynya formed due to the wind action.

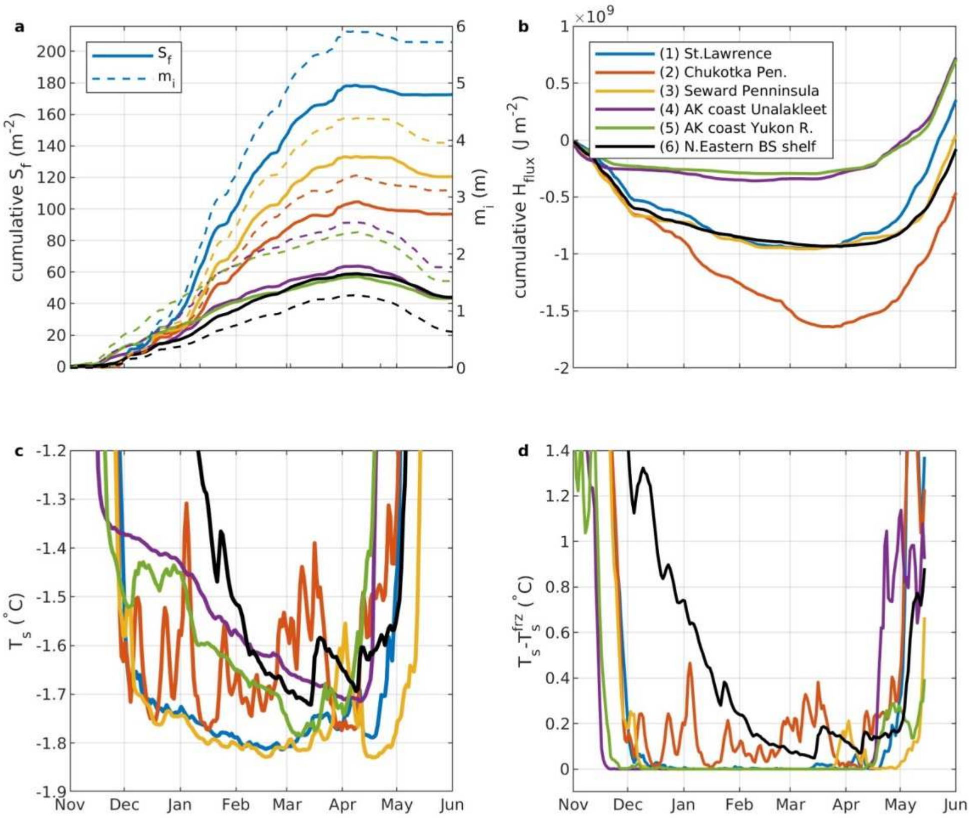

Figure 15. **a** *area-averaged cumulative salt flux (S_f) for the 6 regions delineated in the map at the top of Figure 6, along with cumulative thermodynamic ice production (m_i),* **b** *area averaged cumulative heat flux* **c** *area averaged sea surface temperature (T_s) and* **d** *difference between T_s and the surface freezing point temperature(T_s^{frz}).*

The source of the warm water can be traced to the Anadyr current. Figure 16 displays several fields from a model transect between the Alaskan and Russian coasts (green dashed line in Figure 1a). The winter averaged velocity normal to the transect shows north-northeastward flow over the Gulf of Anadyr along with southward flow close to the Russian coast and on the eastern shelf (Figure 16b). Although the warm water transport in this bottom layer (Figure 16d) is intermittent due to variation in winds and the Bering Sea-Arctic pressure gradient that sometimes reduce the Anadyr current strength, the presence of above-freezing temperature bottom water on the transect throughout the winter (Figure 16e) suggests that vertical mixing (Figure 16b) remains limited enough to isolate this bottom layer from the surface boundary layer. This is supported by the persistence of stratification in winter in the deepest portion of this transect (panel c). The core of warmer bottom water aligns with the northward current (panel d) and is centered approximately half a degree to the west of the minima in surface salinity (panel c). It is likely that this low surface salinity water, that is a product of ice melt, contributes to maintaining the stratification that allows the warm bottom waters to propagate northward.

The wintertime northward flow of the Anadyr current (for earlier winters) is documented in the literature (Muench et al., 1988; Overland et al., 1996). Muench et al. have noted the transport of above freezing temperature water in the current from the Bering Sea slope to Anadyr Strait in the winter of 1985. Although we have not found recent observations to corroborate the sensible heat characteristics of the modeled Chukotka region polynya, the persistence of a stratified water column in the Anadyr basin through the winter has been mentioned (Coachman and Shigaev, 1992). It is possible that the model overestimates Bering Slope bottom water temperatures, and/or underestimates heat dissipating mixing processes as the current progresses northward. But given that the model resolves the flow well, produces an Anadyr current of reasonable magnitude and shows good agreement with the Bering Sea shelf observations in other regions, it is plausible that the model representation in this region is at least qualitatively correct.

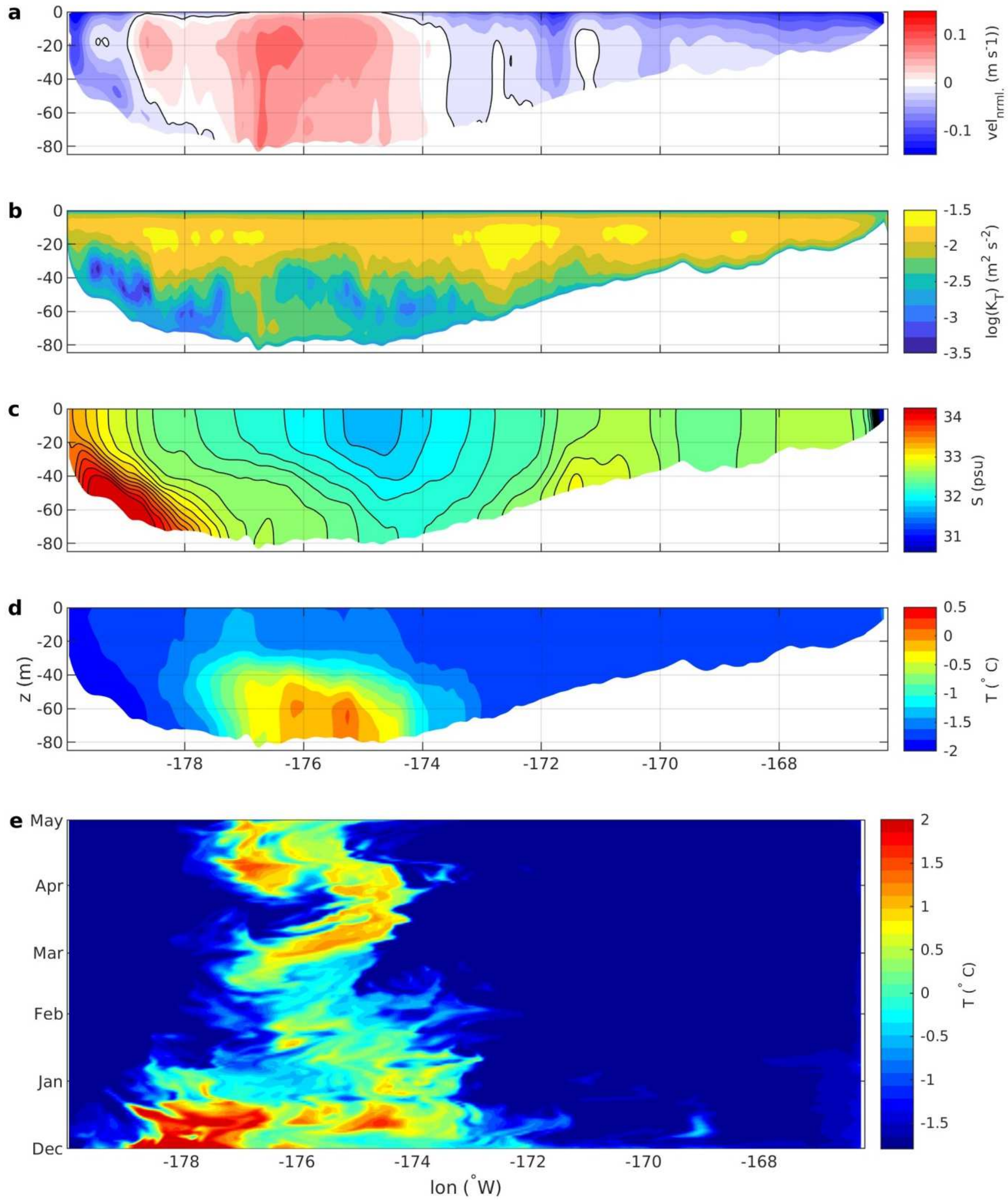

Figure 16. Time-averaged (Dec.1 2009-May 1 2010) ***a*** *section-normal velocity (positive NNE),* ***b*** *log_{10} vertical mixing coefficient,* ***c*** *salinity and* ***d*** *potential temperature along transect 2 (Figure 3) from M_{surfs}. And* ***e*** *near-bottom potential temperature as a function of time and longitudinal position along the transect.*

4.4 Changing characteristics of the mid-to-outer shelf over the winter season

Typical cold winters on the Bering sea shelf are characterized by high sea ice production in the northern coastal regions , advection of ice southward over the broad shelf, where ice production rates are lower, and an outer-shelf region where warm waters from the Bering Sea basin melt a large portion of the sea ice produced over the shelf. In this section, ice and water properties on a model transect from the southern side of St. Lawrence Island to the shelf break north of Zhemchug Canyon (model transect 1 in Figure 1a) are used to elucidate some of the winter characteristics of the shelf. Several of the variables are presented in Figure 18 as functions of the coordinate along the section and time. These analyses are supported by the plots of the individual ice production terms in Figure 17.

Ice is present on this transect from late-November 2009 through mid-May 2010 indicated by the overlaid contours in Figure 17 and Figure 18. The first appearance of ice in the fall occurs as a result of advection (visible in Figure 17 as the presence of ice without any contributions from thermodynamic production terms at the start of the season). Subsequently, thermodynamic production begins particularly strongly in the polynya region by early December. Based on the model, the St. Lawrence polynya, delineated in the figure by lower ice concentrations near the zero of the vertical axis, occupies a region of approximately 0 to 50km from the island coast between the months of December 2009 and April 2010. Intermittent disappearances of the feature over the course of the winter coincide with wind reversals that drive sea ice shoreward (northward). The principle mechanism for ice generation in the polynya region is heat loss from the ocean to the atmosphere indicated by large magnitudes in the w_{ao} and w_{fr} terms (Figure 18a and d). Where ice concentration increases offshore, downwind of the polynya region, sea ice growth occurs mostly through w_{io} though only at a rate approximately one-quarter as large as in the more open water of the polynya. As the ice edge advances offshore, largely due to wind driven advection, it eventually encounters surface waters containing enough heat to cause ice melt (through the negative w_{io} term, see Fig. 17b). In late December through mid-January this occurs approximately 200km south of St. Lawrence island. As the shelf continues to cool, the melt-transition boundary advances farther south behind the ice edge, such that for over much of the winter an approximately 200-km wide band of melting ice is present.

As incoming solar radiation increases and surface air temperatures rise, melt commences over the entire transect in mid-April 2010. The melt is driven both by the atmosphere-ocean heat exchange in the open water portions of each grid cell through the w_{ao} term (Fig. 17a) and at the ice surface through atmosphere-ice exchange (indicated by w_{ai}, Figure 18Fig. 17c). However, from mid-April through the disappearance of all sea ice on this transect, the model predicts that ice formation continues along the underside of the ice at the ice-ocean interface, as the sub-freezing temperature ice continues to extract heat from the ocean. Based on the net thermodynamic ice production in Figure 17e, the transect can be separated into 4 regions in mid-winter. These include a region of net ice production/brine rejection, a region of approximately balanced ice production and melt, a melt region and open water south of the ice edge.

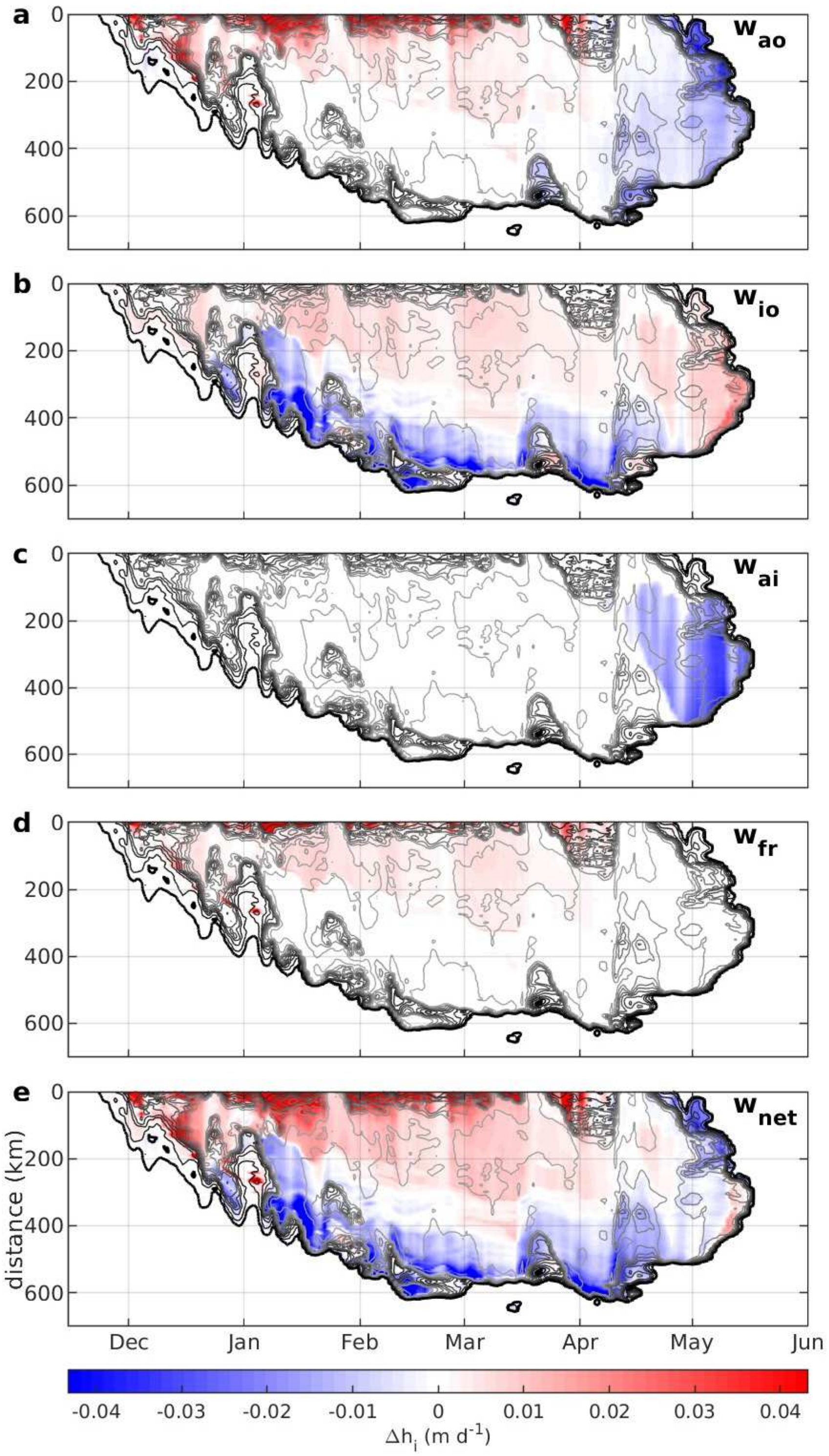

Figure 17. Colors indicate (a)-(d) terms in the thermodynamic ice budget and (e) the net thermodynamic sea ice production as a function of time and distance from St. Lawrence Island along Model Transect 1 (Figure 3). Red indicates sea ice production and blue indicates melt. Black-to-gray contour overlay indicates fractional ice coverage between 0 (black) to 0.95 (light gray) at an interval of 0.1.

Beneath the ice, in the net ice production region, the seasonal impact of the brine rejection is visible in the sea surface salinity distribution and stratification on the transect (Figure 18 a and b). A salinity gradient develops south of St. Lawrence Island over the first part of the winter season due to ice formation both in the polynya and farther offshore, such that by mid-January, the high salinity extends 150km offshore from the island along the transect. Through February, March and April this gradient tends to intensify and advance southward, but remains within the net ice production region delineated in Figure 17d. In this same region, high stratification intermittently develops as the brine water sinks, and is transported laterally away from the island. The variability in the stratification reflects the influence of varying winds and ice production rates. Strong winds tend to mix away the vertical stratification but because they are often oriented to expand the area of the polynya, they can intensify ice formation, brine rejection and consequently horizontal density gradients. As the winds relax, patches of higher stratification often appear (as depicted in Figure 18b) as the horizontal density gradients relax. But other mechanisms restratify the water column in this region as well. The reappearance of lower salinity surface water within 100km of the St Lawrence coast in mid-March 2010, coincident with high stratification in the polynya region, corresponds to a period when a branch of the relatively fresh surface waters of the Anadyr current deflect to the south of the island rather than pass through Anadyr Strait.

In late Dece mber and early January melting occurs on this transect between 150 and 400 km from the coast (Figure 17d) contributing to a decrease in mid-shelf surface salinity that mostly persists throughout the ice covered season (Figure 18a). From February to April an approximately 60 km wide band of unstratified water persists in the midshelf region where neither the presence of ice nor melt is large enough to suppress vertical mixing. As the ice advances farther from shore, the melt region moves farther south generating stratification over a 200km wide swath that extends approximately 200km into the ice cover from the ice edge by mid-March (Figure 18b). Offshore of the ice edge the maximum stratification in the water column is significantly lower than under the ice as the influence of wind mixing is much greater.

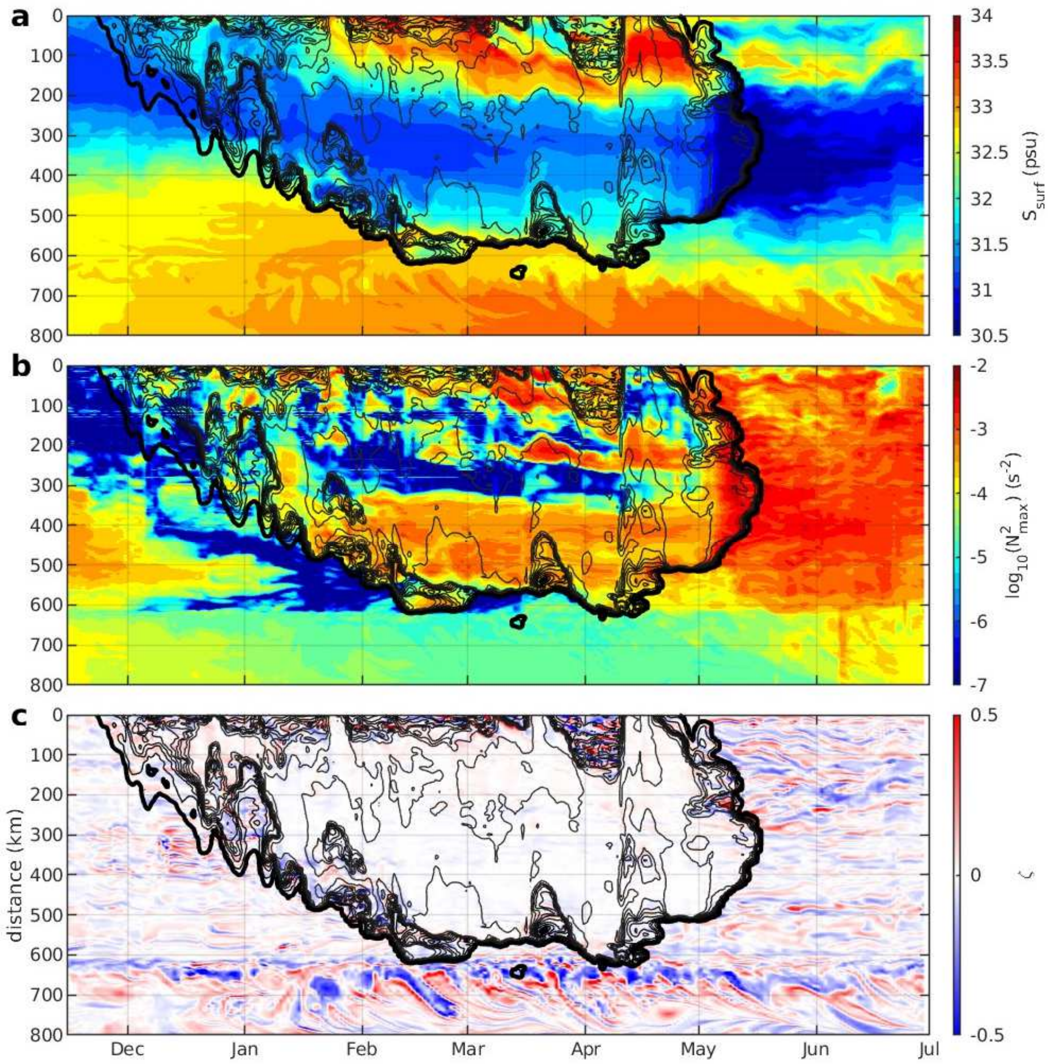

Figure 18. Model fields along Transect 1(Figure 3) as a function of time and distance from St. Lawrence Island. **a** *surface salinity,* **b** *$\log_{10}$ of depth-maximum N^2, and* **c** *mid-depth normalized vorticity ζ. Black-to-gray contour overlay indicates fractional ice coverage between 0 (black) to 0.95 (light gray) with a contouring-interval of 0.1.*

By mid-February, the ice edge on this transect is approaching the shelf break where the warmer waters of the Bering Sea Basin and the strong northwestward flow of the slope current prohibit any farther advance of the ice. For the mid-winter season months of February and March, the shelf temperature and salinity structure remain relatively persistent. Vertical sections of potential temperature, salinity, potential density, vertical mixing coefficient and velocity normal to the transect reinforce the description of the dynamics above (Figure 19). The density gradients are very largely controlled by salinity across the entire transect. Warmer and saltier water underlies colder and fresher water in the broad melt region over the outer shelf. The polynya region is increasingly saltier towards the coast but uniformly cold. Mixing is suppressed most notably over a band approximately 150 km wide in the melt region but is bounded by well-mixed water columns both offshore of the ice edge and in the midshelf region. The density gradients established in the melt region coincide with a low-frequency circulation that transports water in the melt region northwestward consistent with geostrophy. In the ice production region, closer to the St. Lawrence coast, where the brine-induced salinity gradient forms, a weaker southeasterly flow develops (also consistent with geostrophy). Figure 18c shows the mid-depth relative vorticity normalized by the local Coriolis parameter to demonstrate that mesoscale eddy variability beneath the ice coverage is largely suppressed except for locations close to the shoreward (polynya) and seaward ice edges, regardless of stratification. However, once the ice cover melts and stratification intensifies, vigorous eddying motions develop across much of this transect.

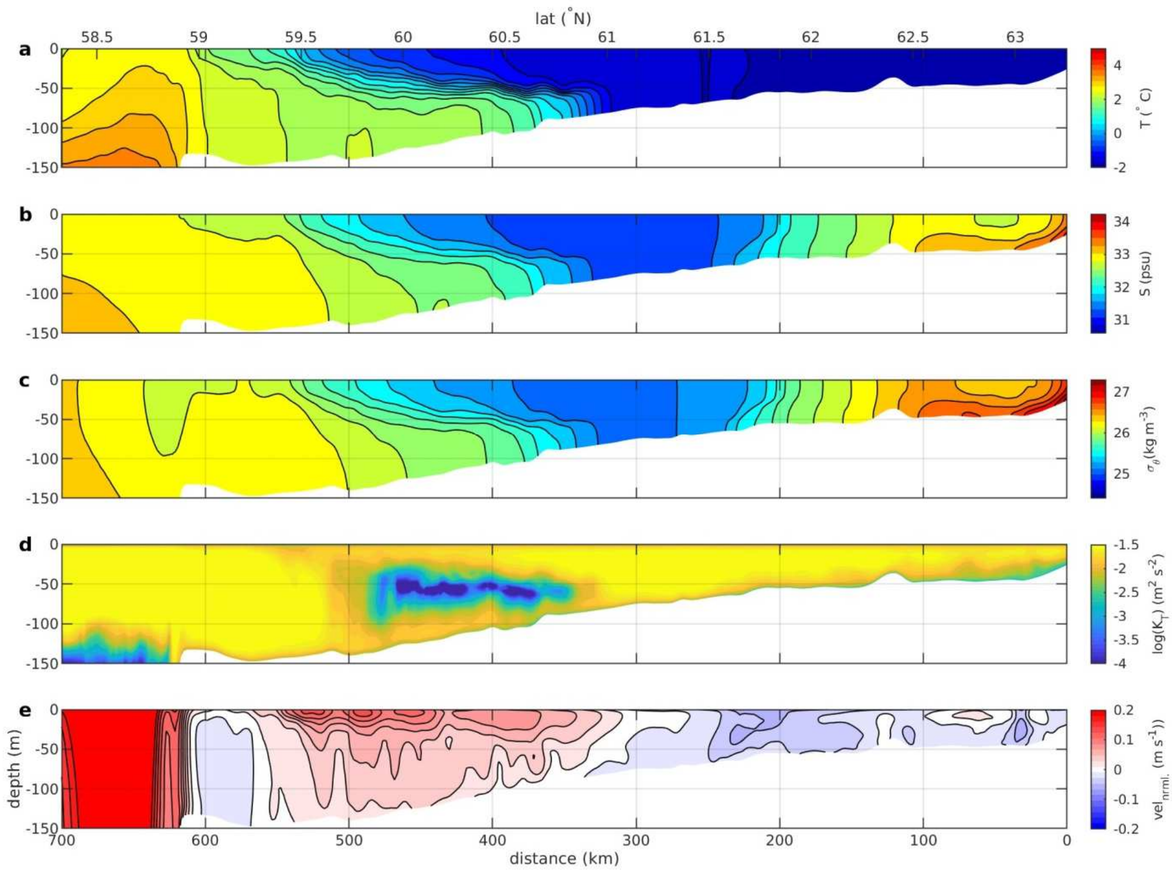

Figure 19. For the St. Lawrence model transect (depicted in Figure 1a), time averaged (Feb 1 – Apr 1 2010) vertical sections of potential temperature (a), salinity (b), potential density (c), vertical diffusivity coefficient (d) and velocity normal to the transect (c, positive northwestward).

5 Summary

In this study we sought to better understand the role of sea ice in the alteration of the eastern Bering Sea salinity distribution over the course of a winter season. For this objective we needed a model that estimated reasonably well the ice coverage, the ice movement and the salinity fluxes between the two water phases. In part 1 of this study we made thermodynamic and dynamic alterations to a relatively unsophisticated sea ice model, and demonstrated the model capability for capturing both the seasonal trend in sea ice coverage over the winter of 2009-10 and the overall movement of the sea ice on shorter time scales. Here, in part 2, the model salt flux parameterization was improved, and reasonable representation of polynya regions was demonstrated.

The model salinity comparisons with mooring and profiler observations were improved significantly by the use of a straightforward salt flux parametrization that depended only on the rate of change of ice mass and the salinity difference between the surface ocean and a fixed sea ice salinity. The model reproduced the increase in salinity on the inner shelf particularly in the northern Bering Sea due to excess ice production relative to melt, while the global HYCOM model failed to reproduce this pattern. South of St. Lawrence Island the model captured the scale of change and variability in salinity as a function of distance from the island that was observed in CTD profiles from April 2010.

The winter of 2009-10 was a relatively cold year for the Bering Sea with large sea ice extent. Under these conditions the model exhibited freshening of the outer shelf (approximately offshore the 75m isobath) and salinization of the inner shelf to the extent that the direction of the positive salinity gradient changes from the offshore direction in the fall to shoreward by May, before riverine input helps to gradually restore the original pattern over the following summer and fall. This evolution results from both a general south-westward movement of the sea ice over the season away from the areas where ice formation was strongest, and from transport of the fresher nearshore waters offshore and to the south. Overall, the volume averaged salinity on the shelf at the end of the melt season is nearly the same as it was before the onset of ice coverage suggesting that salt and ice exchanges with the Arctic and the Bering Shelf slope were negligible or counterbalancing. Future studies of years with more limited ice extent will be beneficial for determining if no net change in shelf salinity is typical or if interannual variability might be expected.

The model produces seasonally averaged anti-cyclonic circulation of both sea ice and ocean waters on the Bering Sea shelf. This leads to recirculation of meltwater northward in the Anadyr Basin and also transport of warm salty bottom water of slope origin in the Anadyr current, causing the deeper waters of the Anadyr basin to remain stratified over much of the winter. Unfortunately, there are few observations available to validate the vertical structure produced by the model in this region.

Coastal polynyas contribute significantly to the redistribution of salinity over the winter season, with the polynya on the south side of St. Lawrence Island being the largest contributor. But other coastal regions similarly aligned relative to the predominant wind forcing, for example, along the south side of the Chukotka and Seward Peninsulas, also frequently exhibited increased open water. Interestingly, ice production and brine rejection were comparatively low in the Chukotka polynya region in the model despite frequent high open water area, because of its exposure to the relatively warmer water being transported northward in the Anadyr current (giving it some characteristics of a sensible heat polynya).

Some discrepancies in nearshore ice coverage between the model and observations were found in the vicinity of the Yukon river outflow where the model at times failed to capture the polynya geometry. These occurrences often appeared to be associated with times in the observations when ice advection was blocked by promontories of landfast ice. Future work can focus on including parameterizations of sea ice grounding (Lemieux et al., 2015) to improve model performance along these portions the Alaskan coast.

Examination of the water column on a transect from the south side of St. Lawrence Island to the shelf break illustrate the variability in stratification beneath the ice coverage. On the outer shelf, where ice was melting above warmer and saltier slope-influenced water, the water column was persistently stratified beneath the ice in a band at times over 200km wide. Intermittent stratification also developed due to strong brine rejection in the polynya resulting in patches of stratified water within 200 km of the south side of the island. The mid-shelf, where neither freezing nor melting processes dominated, was most frequently unstratified.

Despite the encouraging performance of this coupled model, further refinements are warranted. One of these is to more accurately represent the influx of sea ice from the Arctic Ocean. In general, an ice bridge forms north of Bering Strait that acts to inhibit the inflow of arctic ice, but the model has no mechanism presently to emulate this effect. Consequently, the model may be significantly overestimating this effectively freshwater input to the Bering Sea shelf with Arctic ice. A second improvement involves allowing the salinity of the sea ice to vary spatially and temporally. Sea ice has been found to only gradually reject brine over the first couple weeks after its formation. In the Bering Sea, that ice may be advected a significant distance away from where it was formed over that time. Consequently, the model may be somewhat overestimating the brine rejection in polynya regions and underestimating the rejection farther offshore. Nonetheless, even a limited coupled sea ice ocean model, such as the one presented here, can help to elucidate the rich and changing dynamics of the Bering Sea shelf.

Acknowledgements: This research was partially supported by NOAA Total Water Initiative and NASA grant NNX13AD89G. Satellite data was obtained the ASI data repository (https://seaice.uni-bremen.de/start/data-archive/).

Bibliography

Andersen, S., Breivik, L.A., Eastwood, S., Godoy, O., Lind, M., Porcires, M., Schyberg, H., 2007. Ocean & sea ice SAF sea ice product manual version 3.5.

Babb, D.G., Galley, R.J., Asplin, M.G., Lukovich, J.V., Barber, D.G., 2013. Multiyear sea ice export through the Bering Strait during winter 2011–2012. J. Geophys. Res. Oceans 118, 5489–5503. https://doi.org/10.1002/jgrc.20383

Budgell, W.P., 2005. Numerical simulation of ice-ocean variability in the Barents Sea region. Ocean Dyn. 55, 370–387. https://doi.org/10.1007/s10236-005-0008-3

Chassignet, E.P., Hurlburt, H.E., Smedstad, O.M., Halliwell, G.R., Hogan, P.J., Wallcraft, A.J., Baraille, R., Bleck, R., 2007. The HYCOM (HYbrid Coordinate Ocean Model) data assimilative system. J. Mar. Syst., Marine Environmental Monitoring and PredictionSelected papers from the 36th International Liège Colloquium on Ocean Dynamics36th International Liège Colloquium on Ocean Dynamics 65, 60–83. https://doi.org/10.1016/j.jmarsys.2005.09.016

Cheng, W., Curchitser, E., Ladd, C., Stabeno, P., Wang, M., 2014. Influences of sea ice on the Eastern Bering Sea: NCAR CESM simulations and comparison with observations. Deep Sea Res. Part II Top. Stud. Oceanogr. 109, 27–38. https://doi.org/10.1016/j.dsr2.2014.03.002

Clement, J.L., Maslowski, W., Cooper, L.W., Grebmeier, J.M., Walczowski, W., 2005. Ocean circulation and exchanges through the northern Bering Sea—1979–2001 model results. Deep Sea Res. Part II Top. Stud. Oceanogr., The Western Arctic Shelf-Basin Interactions (SBI) Project 52, 3509–3540. https://doi.org/10.1016/j.dsr2.2005.09.010

Clement Kinney, J., Maslowski, W., Okkonen, S., 2009. On the processes controlling shelf–basin exchange and outer shelf dynamics in the Bering Sea. Deep Sea Res. Part II Top. Stud. Oceanogr., The Western Artic Shelf-Basin Interactions (SBI)Project, Vol.2 56, 1351–1362. https://doi.org/10.1016/j.dsr2.2008.10.023

Coachman, L.K., Shigaev, V.V., 1992. Northern Bering-Chukchi Sea Ecosystem: The Physical Basis, in: Nagel, P.A. (Ed.), Results of the Third Joint US-USSR Bering & Chukchi Seas Expedition (BERPAC): Summer 1988. U.S. Fish and Wildlife Service, pp. 17–27.

Danielson, S., Aagaard, K., Weingartner, T., Martin, S., Winsor, P., Gawarkiewicz, G., Quadfasel, D., 2006. The St. Lawrence polynya and the Bering shelf circulation: New observations and a model comparison. J. Geophys. Res. 111. https://doi.org/10.1029/2005JC003268

Danielson, S., Hedstrom, K., Aagaard, K., Weingartner, T., Curchitser, E., 2012a. Wind-induced reorganization of the Bering shelf circulation. Geophys. Res. Lett. 39. https://doi.org/10.1029/2012GL051231

Danielson, S., Weingartner, T., Aagaard, K., Zhang, J., Woodgate, R., 2012b. Circulation on the central Bering Sea shelf, July 2008 to July 2010. J. Geophys. Res. Oceans 117, n/a-n/a. https://doi.org/10.1029/2012JC008303

Donlon, C.J., Martin, M., Stark, J., Roberts-Jones, J., Fiedler, E., Wimmer, W., 2012. The Operational Sea Surface Temperature and Sea Ice Analysis (OSTIA) system. Remote Sens. Environ., Advanced Along Track Scanning Radiometer(AATSR) Special Issue 116, 140–158. https://doi.org/10.1016/j.rse.2010.10.017

Durski, S.M., Kurapov, A.L., 2019. A high-resolution coupled ice-ocean model of winter circulation on the bering sea shelf. Part I: Ice model refinements and skill assessments. Ocean Model. 133, 145–161. https://doi.org/10.1016/j.ocemod.2018.11.004

Durski, S.M., Kurapov, A.L., Zhang, J., Panteleev, G.G., 2016. Circulation in the Eastern Bering Sea: Inferences from a 2-km-resolution model. Deep Sea Res. Part II Top. Stud. Oceanogr. 134, 48–64. https://doi.org/10.1016/j.dsr2.2015.02.002

Griewank, P.J., Notz, D., 2015. A 1-D modelling study of Arctic sea-ice salinity. The Cryosphere 9, 305–329. https://doi.org/10.5194/tc-9-305-2015

Harder, M., Lemke, P., 2013. Modelling the Extent of Sea Ice Ridging in the Weddell Sea, in: The Polar Oceans and Their Role in Shaping the Global Environment. American Geophysical Union (AGU), pp. 187–197. https://doi.org/10.1029/GM085p0187

Hunke, E.C., 2001. Viscous–Plastic Sea Ice Dynamics with the EVP Model: Linearization Issues. J. Comput. Phys. 170, 18–38. https://doi.org/10.1006/jcph.2001.6710

Hunke, E.C., Dukowicz, J.K., 1997. An Elastic–Viscous–Plastic Model for Sea Ice Dynamics. J. Phys. Oceanogr. 27, 1849–1867. https://doi.org/10.1175/1520-0485(1997)027<1849:AEVPMF>2.0.CO;2

Hunt, G.L., Stabeno, P.J., 2002. Climate change and the control of energy flow in the southeastern Bering Sea. Prog. Oceanogr. 55, 5–22. https://doi.org/10.1016/S0079-6611(02)00067-8

Kawai, Y., Osafune, S., Masuda, S., Komuro, Y., 2018. Relations between salinity in the northwestern Bering Sea, the Bering Strait throughflow and sea surface height in the Arctic Ocean. J. Oceanogr. 74, 239–261. https://doi.org/10.1007/s10872-017-0453-x

Ladd, C., Stabeno, P.J., 2012. Stratification on the Eastern Bering Sea shelf revisited. Deep Sea Res. Part II Top. Stud. Oceanogr., Understanding Ecosystem Processes in the Eastern Bering Sea 65, 72–83. https://doi.org/10.1016/j.dsr2.2012.02.009

Lemieux, J.-F., Tremblay, L.B., Dupont, F., Plante, M., Smith, G.C., Dumont, D., 2015. A basal stress parameterization for modeling landfast ice. J. Geophys. Res. Oceans 3157–3173. https://doi.org/10.1002/2014JC010678@10.1002/(ISSN)2169-9291.FAMOS1

Mauch, M., Durski, S.M., Kurapov, A.L., 2018. Connectivity of the Aleutian North Slope Current and Bering Sea Basin Waters at the Level of the Subsurface Temperature Maximum: A Modeling Study. J. Geophys. Res. Oceans 123, 8608–8623. https://doi.org/10.1029/2018JC014097

Mellor, G.L., Kantha, L., 1989. An ice-ocean coupled model. J. Geophys. Res. Oceans 94, 10937–10954. https://doi.org/10.1029/JC094iC08p10937

Mesinger, F., DiMego, G., Kalnay, E., Mitchell, K., Shafran, P.C., Ebisuzaki, W., Jović, D., Woollen, J., Rogers, E., Berbery, E.H., Ek, M.B., Fan, Y., Grumbine, R., Higgins, W., Li, H., Lin, Y., Manikin, G., Parrish, D., Shi, W., 2006. North American Regional Reanalysis. Bull. Am. Meteorol. Soc. 87, 343–360. https://doi.org/10.1175/BAMS-87-3-343

Muench, R.D., Schumacher, J.D., Salo, S.A., 1988. Winter currents and hydrographic conditions on the northern central Bering Sea shelf. J. Geophys. Res. Oceans 93, 516–526. https://doi.org/10.1029/JC093iC01p00516

Overland, J.E., Stabeno, P.J., Salo, S., 1996. Direct evidence for northward flow on the northwestern Bering Sea shelf. J. Geophys. Res. Oceans 101, 8971–8976. https://doi.org/10.1029/96JC00205

Pease, C., 1980. Eastern Bering Sea Ice Processes. Mon. Weather Rev. - MON WEATHER REV 108. https://doi.org/10.1175/1520-0493(1980)108<2015:EBSIP>2.0.CO;2

Schumacher, J.D., Aagaard, K., Pease, C.H., Tripp, R.B., 1983. Effects of a shelf polynya on flow and water properties in the northern Bering Sea. J. Geophys. Res. Oceans 88, 2723–2732. https://doi.org/10.1029/JC088iC05p02723

Semtner, A.J., 1976. A Model for the Thermodynamic Growth of Sea Ice in Numerical Investigations of Climate. J. Phys. Oceanogr. 6, 379–389. https://doi.org/10.1175/1520-0485(1976)006<0379:AMFTTG>2.0.CO;2

Spreen, G., Kaleschke, L., Heygster, G., 2008. Sea ice remote sensing using AMSR-E 89-GHz channels. J. Geophys. Res. Oceans 113, C02S03. https://doi.org/10.1029/2005JC003384

Stabeno, P., Sonnerup, R., Mordy, C., Whitledge, T., Salo, S., 2011. Polar Sea 10-01 CTD and Nutrient Data. Version 1.0. https://doi.org/10.5065/D6J1015W

Stabeno, P.J., Farley Jr., E.V., Kachel, N.B., Moore, S., Mordy, C.W., Napp, J.M., Overland, J.E., Pinchuk, A.I., Sigler, M.F., 2012a. A comparison of the physics of the northern and southern shelves of the eastern Bering Sea and some implications for the ecosystem. Deep Sea Res. Part II Top. Stud. Oceanogr., Understanding Ecosystem Processes in the Eastern Bering Sea 65–70, 14–30. https://doi.org/10.1016/j.dsr2.2012.02.019

Stabeno, P.J., Kachel, N.B., Moore, S.E., Napp, J.M., Sigler, M., Yamaguchi, A., Zerbini, A.N., 2012b. Comparison of warm and cold years on the southeastern Bering Sea shelf and some implications for the ecosystem. Deep Sea Res. Part II Top. Stud. Oceanogr., Understanding Ecosystem Processes in the Eastern Bering Sea 65–70, 31–45. https://doi.org/10.1016/j.dsr2.2012.02.020

Stringer, W.J., Groves, J.E., 1991. Location and Areal Extent of Polynyas in the Bering and Chukchi Seas. Arctic 44, 164–171.

Sullivan, M.E., Kachel, N.B., Mordy, C.W., Salo, S.A., Stabeno, P.J., 2014. Sea ice and water column structure on the eastern Bering Sea shelf. Deep Sea Res. Part II Top. Stud. Oceanogr. 109, 39–56. https://doi.org/10.1016/j.dsr2.2014.05.009

Tartinville, B., Campin, J.-M., Fichefet, T., Goosse, H., 2001. Realistic representation of the surface freshwater flux in an ice–ocean general circulation model. Ocean Model. 3, 95–108. https://doi.org/10.1016/S1463-5003(01)00003-8

Thorson, J.T., Fossheim, M., Mueter, F.J., Olsen, E., Lauth, R.R., Primicerio, R., Husson, B., Marsh, J., Dolgov, A., Zador, S.G., n.d. Comparison of Near-bottom Fish Densities Show Rapid Community and Population Shifts in Bering and Barents Seas [WWW Document]. Arct. Program Rep. Card Update 2019. URL https://arctic.noaa.gov/Report-Card/Report-Card-2019/ArtMID/7916/ArticleID/845/Comparison-of-Near-bottom-Fish-Densities-Show-Rapid-Community-and-Population-Shifts-in-Bering-and-Barents-Seas (accessed 7.9.20).

Vancoppenolle, M., Fichefet, T., Goosse, H., Bouillon, S., Madec, G., Maqueda, M.A.M., 2009. Simulating the mass balance and salinity of Arctic and Antarctic sea ice. 1. Model description and validation. Ocean Model. 27, 33–53. https://doi.org/10.1016/j.ocemod.2008.10.005

Woodgate, R., Weingartner, T., 2015. Temperature, salinity, velocity including ADCP ice tracking, and bottom pressure collected by Bering Strait Moorings A1W, A1, A1E, A2W, A2, A4W, A4, A3 from 2009-08-26 to 2010-08-03. (NCEI Accession 0138582).

Woodgate, R.A., 2018. Increases in the Pacific inflow to the Arctic from 1990 to 2015, and insights into seasonal trends and driving mechanisms from year-round Bering Strait mooring data. Prog. Oceanogr. 160, 124–164. https://doi.org/10.1016/j.pocean.2017.12.007

Woodgate, R.A., 2011. Physical, biological and optical oceanographic data collected from moorings deployed in the Bering Strait from 08/27/2007 to 09/02/2009. (NCEI Accession 0062860).

Woodgate, R.A., Stafford, K.M., Prahl, F.G., 2015. A Synthesis of Year-Round Interdisciplinary Mooring Measurements in the Bering Strait (1990–2014) and the RUSALCA Years (2004–2011). Oceanography 28, 46–67. https://doi.org/10.2307/24861901

Zhang, J., Woodgate, R., Mangiameli, S., 2012. Towards seasonal prediction of the distribution and extent of cold bottom waters on the Bering Sea shelf. Deep Sea Res. Part II Top. Stud. Oceanogr., Understanding Ecosystem Processes in the Eastern Bering Sea 65, 58–71. https://doi.org/10.1016/j.dsr2.2012.02.023

Zhang, J., Woodgate, R., Moritz, R., 2010. Sea Ice Response to Atmospheric and Oceanic Forcing in the Bering Sea. J. Phys. Oceanogr. 40, 1729–1747. https://doi.org/10.1175/2010JPO4323.1

Appendix 1 Adjustment of the salt flux parameterization

In the original Mellor and Kantha paper (1989), referred to here as MK, the salt flux F_S into the ocean is parameterized to depend on the salinity difference between the near-surface ocean (S_{so}) and the molecular sublayer beneath the ice (S_{ms}), along with a coefficient that accounts for the surface boundary layer properties,

$$F_S = -K_S \frac{\partial S}{\partial z} = C_{S_z}(S_{ms} - S_{so}) \qquad z \to 0 \tag{A.1}$$

$$\mathrm{C_{S_z}} = \frac{\mathrm{u_\tau}}{\mathrm{P_{rt}k^{-1}}\, ln\left(\frac{\mathrm{z}}{\mathrm{z_o}}\right) + \mathrm{B_S}} \tag{A.2}$$

where C_{Sz} is

and

$$B_s = \mathrm{b}\left(\frac{z_o u_\tau}{\nu}\right)^{1/2} \mathrm{Sc}^{2/3}. \tag{A.3}$$

In the equations above, $\mathrm{P_{rt}}$ is the turbulent Prandtl number, k is vonKarman's constant, z is depth, z_o is roughness length and $\mathrm{u_\tau}$ is a friction velocity. In MK, A.1 must match the flux between the molecular sublayer and the sea ice,

$$\mathrm{F_S} = (w_\mathrm{O} + c_i r_{mw})(S_{ms} - S_i) - (1 - c_i)(\dot{P} - \dot{E})\boldsymbol{S_{ms}}. \tag{A.4}$$

where r_{mw} is the rate of runoff from surface melt ponds due to contributions from ice melt, snow melt and precipitation. Here,

$$w_o = c_i w_{io} + (1 - c_i) w_{ao} \tag{A.5}$$

As noted in Appendix B of MK, with some approximation a system of equations can be solved to obtain the salt and heat fluxes, ice production rates and molecular sublayer temperature and salinity. But they conclude that it is 'numerically simpler' to estimate the ice production and loss terms from the heat fluxes, determine T_{ms} from S_{ms}, F_T from the temperature analog to equation (1), and combine equations A.1 and A.4 to give the molecular sublayer salinity as

$$S_{ms} = \frac{C_{S_z} S_{so} - w_o S_i + c_i r_{mw} S_i}{C_{S_z} - w_o + c_i r_{mw} + (1 - c_i)(\dot{\mathrm{P}} - \dot{\mathrm{E}})}. \tag{A.6}$$

This expression for S_{ms} is applied in the $\mathrm{M_{MKorig}}$ model setup discussed above.

In the ROMS implementation of this parameterization inherited for use in part 1 of this study, a coding error or perhaps some undocumented modifications to equation A.6 had been made, such that the molecular sublayer salinity was coded as

$$S_{ms} = \frac{C_{S_z} S_{so} - w_{io} S_i - w_{ai}|_{<0} S_i}{C_{S_z} - w_{io} + w_{ai}|_{<0} + r_{mw}}, \tag{A.7}$$

where $w_{ai}|_{<0}$ represents min(w_{ai},0). The total salt flux in a grid cell was estimated as

$$\mathbf{F_S} = (\boldsymbol{w_\mathrm{O}} + \boldsymbol{c_i w_{ai}}|_{<0})(\boldsymbol{S_{ms}} - \boldsymbol{S_i}) - \boldsymbol{c_i r_{mw} S_i} + (\mathbf{1} - \boldsymbol{c_i})(\dot{\boldsymbol{E}} - \dot{\boldsymbol{P}})\boldsymbol{S_{so}}. \tag{A.8}$$

The model using equations A.7 and A.8, with the aforementioned coding error uncorrected, is referred to as $M_{p1\text{-}Dyn}$ in the manuscript; this formulation is identical to S_{Dyn} discussed in Part 1. It is not obvious and not documented how this parameterization was determined, yet it produces quite reasonable evolution of surface sea ice concentration for the winter of 2009-10, as discussed in Part 1. Variables w_{ao} and c_i are absent, so presumably equation A.7 is based on the assumption that the salinity of the molecular sublayer should be a function of the rates of ice growth/loss and meltwater runoff only in the ice-covered portion of a grid cell. Also, as r_{mw} is often equal to, and redundant with w_{ai} when surface melting of ice is occurring, this equation implies, not unreasonably, that their contribution to the molecular sublayer characteristics should be weighted differently than changes due to melting at the ice-ocean interface.

Whether M_{MKorig} or $M_{p1\text{-}Dyn}$ is utilized, questions arise regarding conservation of salt over a freeze/melt cycle. For example, due to the dependence on wind stress in C_{S_z} , the same thermodynamic production of ice will lead to a different salt flux under different wind conditions. Additionally with $M_{p1\text{-}Dyn}$, the salinity flux associated with the same production/melt of ice will differ depending on which mechanism (w_{ao}, w_{io} , w_{ai}, etc.) it is associated with. Over a freeze-melt season in a closed domain, neither formulation assures that the net freshwater flux during the melt season will balance the total brine rejection during freeze up.

The primary motivation of this part of the study is to evaluate the evolution of the Eastern Bering Sea shelf salinity structure over the winter. But salinity fields obtained using $M_{p1\text{-}Dyn}$ (S_{dyn}) in Part 1 exhibited poor agreement with salinity observations from shelf moorings and CTD profiles for the winter of 2009-10. The alternative of using M_{MKorig} did not prove beneficial either. Even small changes in S_{ms} significantly altered the evolution of ice concentration in the Bering Sea. So in order to preserve the quality of the solution in terms of ice concentration found in Part 1, simple alternative parameterizations for F_S are considered here, while the coded formulation for S_{ms} (A.7) is retained. Despite the ambiguity of its origins, we retain this parameterization in calculating the molecular sublayer temperature and ice-temperature evolution, but decouple it from the calculation of salt flux.

In principle, formulating a set of simultaneous equations that capture the interdependence of the interfacial salinities, temperatures, heat fluxes and ice production in a consistent manner may be possible but it is numerically challenging and beyond the scope of this work. For the purposes here, we opt for simple alternatives to the flux formulation outlined above that reproduce the ice formation/melt rates obtained in previous simulations while improving the salt flux estimates and overall salt conservation. As presented in 2.1.3 above, the total surface salt flux in the principle simulations discussed here is (**8**), with the ice-ocean salt flux being given by (**5**) for M_{cons} and (**7**) for M_{surfS}.

Appendix 2 1-dimensional test case

An idealized test of these salt flux parameterizations is presented here to summarize the impact of the model modifications mentioned above. We simulate a seasonal cycle in a spatially uniform, doubly periodic domain (effectively a 1-dimensional water column simulation), representative of the central Bering Sea shelf. The initial conditions and forcing are identical to those used in the full 3-dimensional model at approximately the position of the N55 Bering Sea shelf mooring on the 55m isobath (62°N, 172.6°W). The maximum allowable value of c_i is set to 0.97 in these experiments to ensure that lateral ice melt, w_{ao}, can contribute. (Without this limit the sea ice uniformly thins over the entire grid cell during the melt season, and the role of w_{ao} in the salt flux cannot be analyzed.) Simulations are performed using 5 different salt flux parameterizations. These include $M_{p1\text{-}Dyn}$, M_{MKorig}, M_{consS}, M_{surfS} and a case in which ice formation and melt do not contribute to the surface salt flux M_{precip} ($\mathrm{F_S} = (\dot{E} - \dot{P}) S_{so}$). In this case, ice still forms and melts comparably to the other four cases, but ocean surface salinities change much less.

In these 1-dimensional simulations, c_i changes rapidly, reaching a maximum by early January while the mass of ice (or h_i, the cell-averaged thickness) gradually increases into May (Figure 20a). The ice cover persists longer than in the Bering Sea simulations for several reasons. First, by not allowing c_i to reach a value of 1, the direct atmosphere-ocean heat exchange continues through the winter enhancing sea ice production. Second, the doubly periodic boundary conditions provide no lateral exchange with warmer water as on the actual Bering Sea shelf, and no possibility for the sea ice field to diverge and allow increased heat absorption by the ocean.

The $M_{p1\text{-}Dyn}$ idealized simulation produces significantly thicker sea ice and consequently a longer melt season than any of the other cases (Figure 20), largely due to the code error mentioned above. The over-estimated cooling of the water column compounded by the maximum set on c_i leads to excessive frazil ice accretion. The M_{MKorig} case produces more ice than either M_{consS} or M_{surfS}, due primarily to higher ice production between mid-December 2009 and mid-January 2010. During this period, the M_{MKorig} estimate of S_{ms} (A.6) is significantly closer to the sea surface salinity than that for the cases using equation A.7. This leads to a fresher water column and increased frazil ice production which largely accounts for the difference.

M_{precip} demonstrates that the net effect of evaporation and precipitation over the season is to slightly freshen the water column (Figure 20b). The abrupt drop in salinity with the final melting of the ice in late June is due to the flushing of fresh snowmelt from the ice surface. The changes in water column salinity due to ice formation and melt are much larger. In $M_{p1\text{-}Dyn}$ the excess ice production (associated with the w_{fr} term) is not accompanied by a commensurate increase in salt flux. So when melting occurs (through the w_{ao}, w_{ai} and w_{io} terms), the freshwater flux exceeds the brine injection, causing a net loss of salt in the water column over the winter (Figure 20b). The M_{MKorig} experiment produces a net increase in salinity over the season. This is presumably due in part to an underestimate of S_{ms} during the melt season. But it is also likely due to the assumption in equation A.4 that all surface runoff has a salinity of S_i (an overestimate for the melted snow). The net change in salinity in both M_{consS} and M_{surfS} is very similar to the M_{precip} case, indicating that these schemes are conserving salinity well over the ice formation/melt cycle. Though indiscernible in Figure 20b, S_{avg} for M_{consS} is approximately 0.01 higher than for M_{surfS} at the end of the winter season due to the role of S_{so} in the salt flux parameterization (**7**).

Comparison of Figure 20b with the top panel of Figure 9a shows that for the one-dimensional study $M_{p1\text{-}Dyn}$ leads to a net decrease in salinity, while in the full eastern Bering Sea simulation it leads to a net increase on the shelf. This results from both the code error and the inconsistencies of that formulation. S_{ms} in this formulation, which plays a role in determining the magnitude of the salt flux, is a function of w_{io} and w_{ai} but not w_{ao}. So, w_{ao} affects the salt flux associated with freezing or melting differently than the other mechanisms. As the contributing mechanisms differ between the full shelf and the idealized 1-dimensional case, so too does the error in the net salt flux over the winter season.

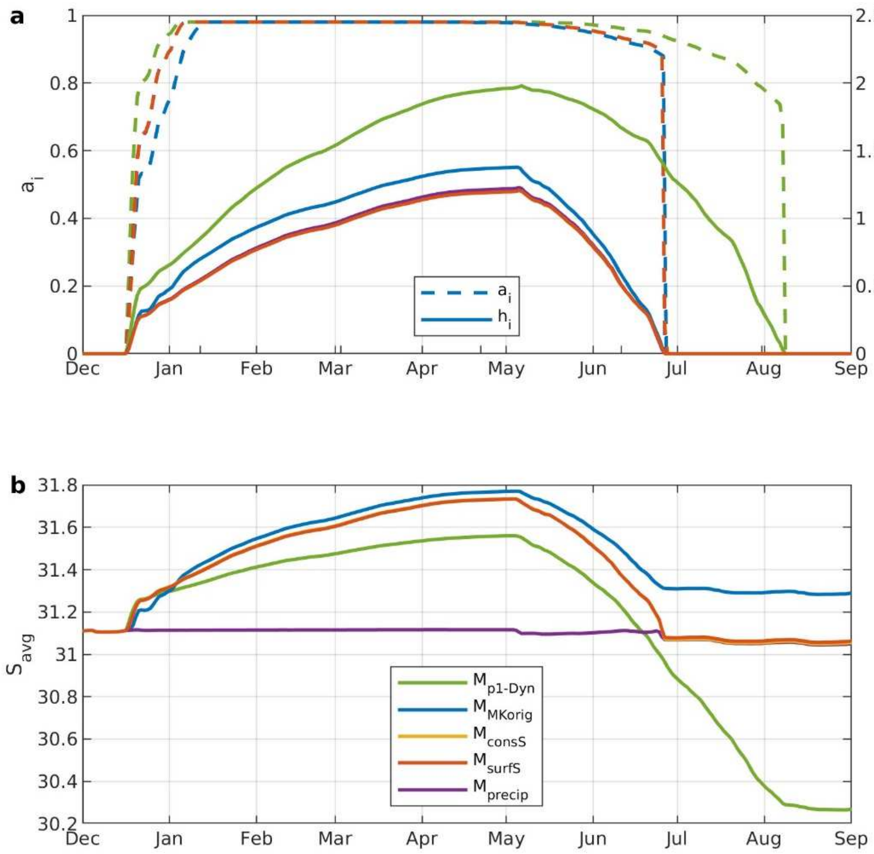

Figure 20 **a** *Ice concentration (solid lines) and grid cell-averaged ice thickness (dashed lines), and* **b** *depth averaged salinity, for idealized 1-dimensional water column simulations representative of the midshelf from December 2009 to September 2010. The yellow and purple lines in panel* ***a*** *and the yellow line in panel* ***b*** *are not discernible because they lay nearly directly beneath the red line.*